Eastward-Propagating Planetary Waves Prior to Sudden Stratospheric Warmings

Christian Rhodes[1], Varavut Limpasuvan[1], Yvan Orsolini[2]

[1]School of Coastal and Marine Systems Science, Coastal Carolina University, Conway, South Carolina, USA, [2]Norwegian Institute for Air Research (NILU), Kjeller, Norway.

Corresponding author: Christian Rhodes (ctrhodes@coastal.edu)

Key Points:

- Before major sudden stratospheric warmings, planetary and gravity waves form a middle atmosphere double-maxima zonal wind structure.
- The double-maxima wind configuration favors instability planetary wave growth via over-reflection.
- The refractive index of the wintertime middle atmosphere reveals an inherent bias to produce instability waves with eastward phase speeds.

Abstract

The sources and characteristics of the slow eastward-propagating planetary waves (EPWs) were investigated prior to the major sudden stratospheric warming (SSW) events, as observed by the Microwave Limb Sounder (MLS) and simulated by the National Center for Atmospheric Research (NCAR) Whole Atmosphere Community Climate Model (WACCM) with specified dynamics. With a zonal phase speed of ~10 $m \cdot s^{-1}$, these EPWs appeared as wavenumber-1 and -2 perturbations in the boreal stratosphere and mesosphere prior to SSWs with split and displaced polar vortex. Found near the turning and critical layers, these waves were manifestations of an unstable eastward mesospheric flow. These instability waves were investigated from the perspective of over-reflection. A zonal-mean zonal wind structure with local maxima around the upper polar stratosphere and the subtropical mesosphere was commonly found prior to SSW onset as the result of net forcing by gravity and planetary waves. This structure was largely unstable and provided the wave geometry conducive to over-reflection.

1 Introduction

The wintertime structure of the stratosphere and mesosphere arises from the competing effects between net radiative heating and wave forcing (Andrews et al., 1987). The main source of stratospheric variability is upward-propagating planetary waves (PWs) generated in the troposphere by large-scale orography and heat sources (e.g., Charney & Eliassen, 1949; Smagorinsky, 1953). During the Northern Hemisphere (NH) winter, the prevailing eastward flow of the polar night jet allows PWs to propagate into the stratosphere and, upon their dissipation, impact the flow. Above the stratosphere, gravity waves (GWs) from tropospheric sources (e.g., convection, fronts, and small-scale orography) play an important role. In particular, the breaking of upward-propagating GWs with westward phase speeds imposes a strong westward drag on the eastward flow, capping the top of the polar night jet and modulating the polar stratopause (Duck et al., 2001; Leovy, 1964). However, variations in strength and direction of the lower stratospheric winds can usher GWs of different zonal phase speeds into the mesosphere, affecting the gravity wave drag (GWD) distribution near the top of the polar night jet. Overall, the combined influence of GWs and PWs keeps the polar vortex warmer than otherwise under radiative equilibrium.

Occasionally, when the upward PW activity is large, its eventual dissipation in the NH winter polar stratosphere can strongly decelerate the zonal-mean zonal wind ($\bar{u}$). Subsequently, $\bar{u}$ can reverse direction as the polar region undergoes rapid warming (Matsuno, 1971), resulting in a phenomenon called a major sudden stratospheric warming (SSW). Occurring roughly 60% of NH winters (e.g., Butler et al., 2015), SSWs are also characterized by the highly perturbed stratospheric polar vortex becoming split (i.e., split SSW) or highly displaced off the North Pole (i.e., displaced SSW). The impacts of SSWs have been linked to anomalously cold conditions over Europe and Northeast America (e.g., Baldwin & Dunkerton, 2001) and atypical atmospheric perturbations above the stratosphere (Goncharenko et al., 2010; Limpasuvan et al., 2016; Pedatella et al., 2016; Sassi et al., 2016).

The zonal-mean zonal wind structure in the stratosphere and mesosphere can exhibit regions of unusually strong wind shear. There, the flow can become barotropically or baroclinically unstable, leading to the appearance of unstable PWs (e.g., Dickinson, 1973; C. B. Leovy & Webster, 1976; Matthias & Ern, 2018). For shear instability to occur, the generally positive meridional (quasi-geostrophic) potential vorticity gradient ($\bar{q}_\phi$) associated with the

wintertime circulation must become negative (e.g., Salby, 1996). To serve as a source for an instability wave of a certain zonal phase speed (c_x), that region must also contain a critical layer, where the mean zonal flow matches c_x (Dickinson, 1973). Hartmann (1983) used a linear barotropic model and a quasi-geostrophic baroclinic model to examine instabilities of the eastward stratospheric polar night jet. He found that, when the instability was seated on the poleward flank of the jet, the most unstable modes were wavenumber-1 and -2 waves with periods of a few days. When the instability was seated on the mid-latitude flank of the jet, the most unstable modes were wavenumber-1 to -3 waves with periods of a week or more. Manney et al. (1988) suggests that these periods are likely slightly longer in observations since the nonlinear effect of instability tends to weaken and broaden the jet (Pedlosky, 1987). Orsolini & Simon (1995) used a fully nonlinear nondivergent barotropic model to simulate the generation and life cycle of unstable PWs arising from the instability of the polar night jet, as well those arising from the instability of a double jet representing the mesospheric subtropical jet and the upward extension of the stratospheric polar night jet. These authors found similar low-wavenumber instability waves as Hartmann (1983) with periods on the order of days for the single jet case. Planetary-scale vortices developed to expel the low potential vorticity on the poleward flank of the jet into lower latitudes, acting to remove the sign reversal of the meridional potential vorticity gradient. Eddies of higher wavenumbers (3-4) were found in the double-jet case, accelerating and stabilizing the flow between the two zonal wind maxima. Although perturbations of higher wavenumbers have larger growth rates, Hartmann (1983) suggested that low-wavenumber instabilities (given the predominance of low-wavenumber disturbance in the stratosphere) would be more likely to derive energy from an unstable flow than higher wavenumbers.

Prior to the split SSW of January 2009, a couple of studies noted the presence of slow eastward-propagating PWs, hereafter EPWs, in the mesosphere (L. Coy et al., 2011; Iida et al., 2014). Using a high-top forecast model with data assimilation, Coy et al. (2011) suggested that the mesospheric EPWs directly propagated from the troposphere with the underlying bursts of wavenumber-2 PW activity prior to the SSW onset and their eventual dissipation in the lower mesosphere. Using satellite observations, Iida et al. (2014) noted that the EPW appearance before SSW onset could be generated by *in situ* shear instability of the polar night jet. Regardless of their source, EPWs may be a common feature leading up to SSW. In the composite study of Limpasuvan et al. (2016) based on 13 SSW events, a robust signature of zonal wavenumber-1 EPW with an eastward period of around 10 days was clearly evident between 40-60 km and over the polar region, intensifying roughly 10 days before SSW onset (see their Figure 10). However, these authors did not discuss the cause of the wave presence and focused only on the wavenumber-1 westward-travelling wave, developing after the SSW onset. Hence, the exact nature of EPWs and why they occur before SSW onset remain unclear.

In general, propagating PWs can interact with a pre-existing unstable region (where $\bar{q}_\phi$ is negative) and over-reflect (Harnik & Heifetz, 2007). Following Lindzen et al. (1980), **Figure 1** illustrates this scenario for a simplified atmosphere with some assumed $\bar{u}$ vertical profile. Over-reflection occurs when an incident PW reflects from the unstable region with more energy than it initially had (thick arrow). At the turning level (indicated by the $\bar{q}_\phi$ sign change), the incident PW can tunnel through the evanescent region (where the wave amplitude diminishes exponentially with height) before eventually reaching the critical layer (where the squared refractive index n^2 also changes sign). An associated over-transmission occurs when diminished

PW emerges from the critical layer with more energy than the incident PW. In this circumstance, an instability wave can manifest an over-reflected component emanating downward from the turning level and an over-transmitted component emerging from the critical layer (Dickinson, 1973). If the evanescent region is sufficiently thin, the exponentially decaying waves can readily reach the critical layer.

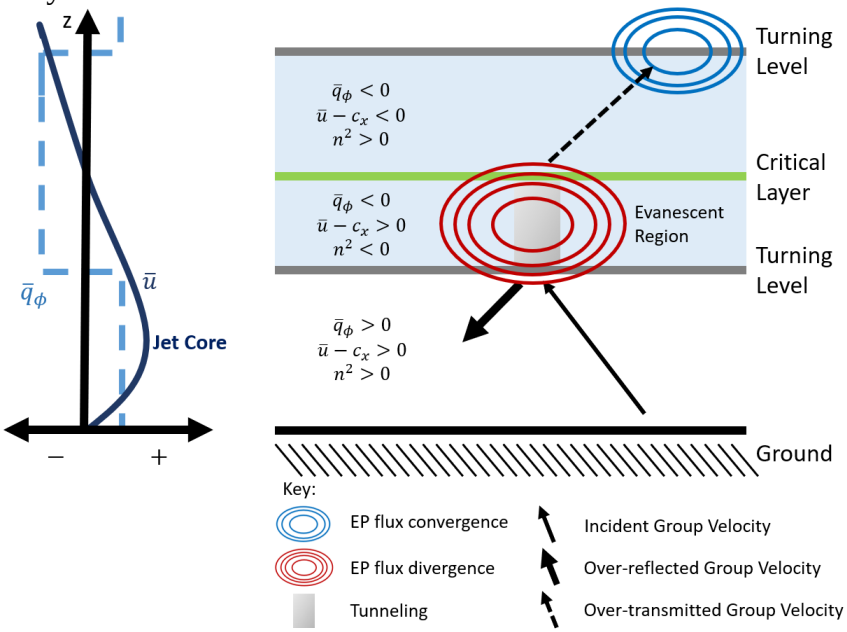

Figure 1. A schematic of PW over-reflection with background $\bar{u}$ and $\bar{q}_\phi$ fields shown on the left with arbitrary magnitudes. On the right, upward-propagating PWs (thin solid arrow) over-reflect at the turning level, resulting in a reflected wave (thick solid arrow) with enhanced energy. A transmitted wave (thin dashed arrow) appears above the critical layer. The light blue shading indicates the negative $\bar{q}_\phi$ region.

Through this over-reflection perspective, instability waves are manifestations of stimulated emissions from the unstable flow region. As such, the upward EPWs burst noted by Coy et al. (2011) and the instability EPWs observed by Iida et al. (2014) prior to SSW may not be independent in the context of Figure 1.

The present study evaluates the source and characteristics of mesospheric EPWs prior to SSWs using a high-top general circulation model and global satellite observations. Based on several SSW events and their composite, we attempt to examine the roles of GWs and PWs in fostering changes in the background mesospheric wind leading up to SSW onset and the EPW presence. Focus is placed on the interplay of wave geometry and the roles of over-reflection and over-transmission with respect to shear instability that manifests as EPWs. To our knowledge, this is the first study to examine the mesospheric instabilities prior to SSW events from such perspective. From the basis of mesosphere-stratosphere coupling prior to SSW, our results may help assess the role of the mesosphere in SSW predictability. Our findings reveal the appearance of robust and unique double-maxima wind structure set up by GWs and PWs prior to SSW. This wind structure is conducive for the occurrence of strong and persistent EPWs. Appearing in the mesosphere as wavenumber-1 and wavenumber-2 perturbations before both split and displaced

SSWs, EPWs are manifestations of shear instability as well as over-reflection by upward-propagating PWs.

2. Methods

2.1 Model and Observations

We utilized the Whole Atmosphere Community Climate Model, Version 4 (WACCM) developed at the National Center for Atmospheric Research (NCAR). As part of the Community Earth System Model Version 1.2, WACCM is an atmosphere-only global chemistry-climate model that extends up to ~145 km (5.1×10^{-6} hPa). Details of WACCM are provided by Marsh et al. (2013). Notable model features include parameterization of GWD generated by convection and fronts as well as mountain stresses which have improved the frequency of SSWs in the Northern Hemisphere (Richter et al., 2010).

WACCM was run in the specified dynamics configuration from 1980 to 2013. Referred to as WACCM-SD, this configuration has a horizontal resolution of 0.95° latitude by 1.25° longitude, 88 vertical levels, and key dynamical variables output daily. The model's temperature and dynamics are constrained up to 50 km with six-hourly Modern-Era Retrospective Analysis for Research and Application (MERRA) Version 2 reanalysis (Gelaro et al., 2017). A linear transition is applied between the nudged output below 50 km and the overlying (fully interactive) free-running region above 60 km.

Model results were compared to observations from the Microwave Limb Sounder (MLS) aboard the polar-orbiting NASA Earth Observing System Aura satellite. Geopotential height are retrieved from the 118-GHz (2.54 mm wavelength) and 234-GHz (1.28 mm wavelength) O_2 spectral lines and temperature from the 118-GHz and 239-GHz (1.23 mm wavelength) O_2 spectral lines. Both variables are useful between 261 hPa and 0.001 hPa (Livesey et al., 2017). Orbiting the Earth ~15 times per day, the satellite provides near-daily global coverage when combining measurements from both the ascending and descending tracks.

2.2 SSW Identification and Classification

SSW identification has been traditionally based on the World Meteorological Organization (WMO) definition, dating back to 1952 when the first SSW was initially observed (Scherhag, 1952). Over the years, variation of this definition has crept into practice (Butler et al., 2015). Studies focused on the coupling between SSW and the mesosphere-lower thermosphere (MLT) region may specialize to SSW events during which the vortex recovery is accompanied by a stratopause elevated above its climatological altitude (Manney et al., 2008). These specialized SSWs with an elevated stratopause are referred to as ES-SSWs. Based on the zonal-mean zonal wind and temperature averaged between 70°N and 90°N during the extended winter, Limpasuvan et al. (2016) identified an ES-SSW event if: (1) the temperature falls below 190 K between 80-100 km, (2) the zonal-mean zonal wind reverses from eastward to westward at 1 hPa and persists longer than 5 days, and (3) the stratopause altitude based on the zonal-mean temperature maximum between 20-100 km exhibits a vertical discontinuity of at least 10 km. With focus on the upper-stratospheric and mesospheric dynamics pertinent in this study, these criteria are used here to identify SSW onset dates and listed in **Table 1**. Between 1984 and 2013, 13 SSW events are identified. To consider the diversity of EPW occurrences, we note in Table 1 how the SSWs were classified (as either split or displaced) based on past studies. We emphasize that the onset is defined based on a zonal-mean zonal wind reversal at 1 hPa.

Onset year (YYYY)	Onset date (MM-DD)	Classification by other studies
1984	02-21	Displaced (Charlton & Polvani, 2007)
1984	12-30	Split (Charlton & Polvani, 2007)
1987	01-22	Displaced (Charlton & Polvani, 2007)
1989	02-19	Split (Charlton & Polvani, 2007)
1995	01-27	Not Present
1997	12-23	Not Present
2002	02-13	Displaced (Charlton & Polvani, 2007)
2003	12-20	Displaced (Kuttippurath & Nikulin, 2012)
2006	01-09	Displaced (Kuttippurath & Nikulin, 2012)
2009	01-22	Split (Manney et al. 2009, Kuttippurath & Nikulin, 2012)
2010	01-24	Displaced (Kuttippurath & Nikulin, 2012)
2012	01-13	Displaced (Chandran et al., 2013)
2013	01-05	Split (Coy & Pawson, 2015)

Table 1. Identification and classification of SSWs from 1979 to 2013. SSW onset dates were defined by the point of wind reversal at 1 hPa**.** Each event identified qualifies as an ES-SSW according to criteria from Limpasuvan et al. (2016). The SSW type was classified by multiple studies (Chandran et al., 2013; Charlton & Polvani, 2007; Lawrence Coy & Pawson, 2015; Kuttippurath & Nikulin, 2012; Manney et al., 2009).

2.3 Data Analyses

EPWs were identified by bandpass filtering specific wavenumbers over a range of eastward phase speeds. Using Fourier transform, a Hanning window spanning 31 days was applied such that subseasonal variations were captured. To alleviate the dampening effect of the Hanning window, the Fourier transform was performed daily such that the window straddled a central date (a sliding window). The Eliassen-Palm (EP) flux was calculated following the formulation in Andrews et al. (1987) and based on 5-day averages of dependent field variables (wind, temperature, etc.). While this inherently filtered out waves with periods < 5 days (or with $c_x > 46$ m·s^{-1} at 60°N), this was well below the expected period of > 14 days (or $c_x < 20$ m·s^{-1} at 30-50°N) suggested by Coy et al. (2011). For MLS, the vertical velocity and vertical fluxes were neglected in the EP flux calculation. Regardless, these components were negligible in the EP flux calculation of the model data.

For MLS, the horizontal winds were calculated from the observed geopotential based on the geostrophic wind approximation shown in Iida et. al, (2014). A running 3-day average was applied to appropriate variables before computing $\bar{q}_\phi$ (O'Neill & Youngblut, 1982):

$$\bar{q}_\phi = 2\Omega cos\phi - \mathrm{R_e^{-1}} \frac{\partial}{\partial \phi}\left(\frac{1}{\cos\phi}\frac{\partial(\bar{\mathrm{u}}\cos\phi)}{\partial\phi}\right) - \frac{R_e f^2}{\bar{\rho}}\frac{\partial}{\partial z}\left(\frac{\bar{\rho}}{N_B^2}\frac{\partial \bar{u}}{\partial z}\right) \quad (1)$$

where ϕ is the latitude, z the log-pressure height, f the Coriolis parameter, N_B the Brunt-Väisälä frequency, $\bar{\rho}$ the zonal-mean atmospheric density, Ω the Earth's angular frequency, and R_e the Earth's radius. In later discussion, we refer to the positive definite first term on the right hand side (RHS) as the "beta term" associated with the gradient of f, the second term as the "barotropic term" associated with horizontal wind curvature, and the third term as the "baroclinic term" associated mainly with the vertical wind curvature. The squared refractive index (n^2) can be used to better understand how PWs of certain zonal wavenumbers (s) and zonal phase speeds (c_x) propagate in $\bar{u}$ (Andrews et al., 1987):

$$n^2 = \frac{\bar{q}_\phi}{R_e(\bar{u} - c_x)} - \left(\frac{s}{R_e\, cos\phi}\right)^2 - \left(\frac{f}{2N_B H}\right)^2 \quad (2)$$

where H is the scale height. PWs tend to propagate towards a large positive squared refractive index and are unable to propagate in regions with a negative squared refractive index. In figures, $\bar{q}_\phi$ and n^2 are nondimensionalized by Ω and R_e^2, respectively.

Following Coy et al. (2011), the presence of a wave with a specific wavenumber was detected if the geopotential height perturbation (GHP) amplitude exceeded 200 m. After binning the geopotential height amplitude by phase speed, the mean phase speed and standard deviation were calculated. A critical layer was identified if the background wind was within 0.05 standard deviations of the mean phase speed and the GHP amplitude exceeded 200 m.

3 January 2009 Split SSW Case

The mesospheric PWs prior to the January 2009 split SSW event are first investigated. A focus on this particular case allows the present study's findings to be substantiated by those of Coy et al. (2011) and Iida et al. (2014). This split SSW event was associated with very strong polar warming of more than 50 K in a matter of days (e.g., Harada et al., 2010).

In WACCM-SD, SSW onset occurs on 22 January 2009 (see Table 1). Evident in **Figure 2**a, the upper-mesospheric zonal-mean zonal winds reversed ~5 days prior to the onset date indicated by the vertical dashed line. The early reversal of the upper-mesospheric wind before SSW onset is also evident in the MLS observations of Iida et al. (2014). In the stratosphere and lower mesosphere, the polar jet strengthened a few days prior to wind reversal. Gold and brown vertical bars in Figure 2a mark selected time slices of the meridional cross-sections of the zonal-mean zonal wind shown in Figures 2c and 2d. The zonal-mean zonal wind climatology (devoid of ES-SSWs listed in Table 1) in Figure 2b is shown for comparison. By 31 December, the eastward winds had strengthened compared to climatology. Furthermore, a double-maxima wind configuration had developed with a distinct eastward mid-latitude core near the stratopause and an eastward low-latitude subtropical core near 80 km, both with speed exceeding 60 $m \cdot s^{-1}$.

Throughout December, GW dissipation capped the eastward jet in the mid- to high-latitudes with local westward drag (blue contours) of more than 80 $m \cdot s^{-1} \cdot day^{-1}$, maintaining the zero-wind line above 80 km.

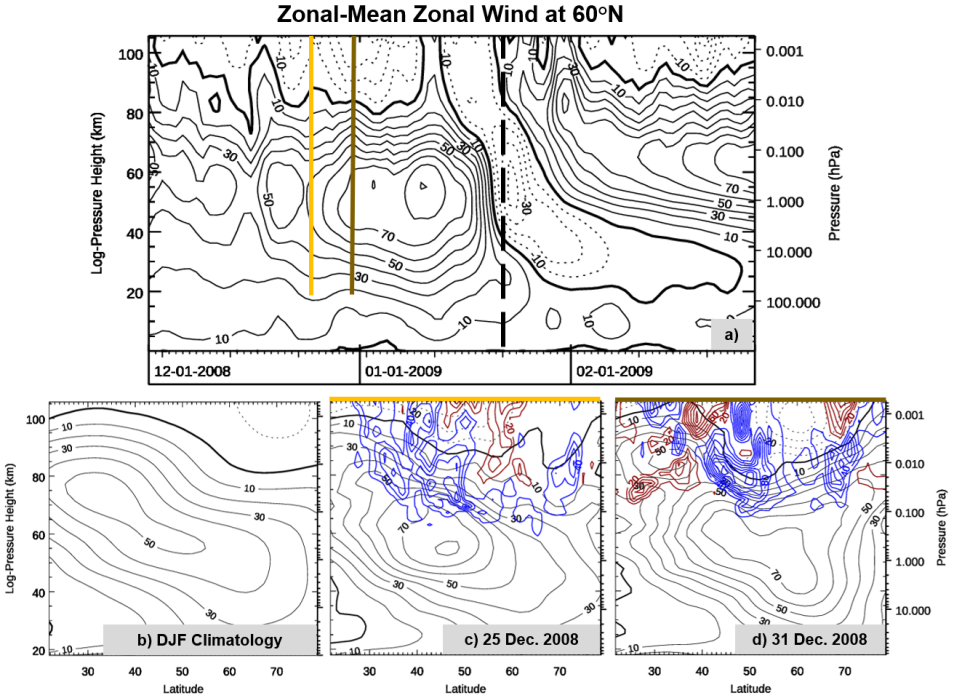

Figure 2. (a) Polar-averaged zonal-mean zonal wind ($\bar{u}$) evolution during the 2009 split SSW event with an onset date of 22 January as indicated by a vertical dashed line. (b) The December-February $\bar{u}$ climatology for the 1980-2013 period without ES-SSWs. (c) and (d) $\bar{u}$ for 25 and 31 December 2008, respectively. For all, the westward (dotted black contour) and eastward (solid thin black contour) wind is contoured every 10 $m \cdot s^{-1}$, with the zero-wind line thickened. Incremented by 20 $m \cdot s^{-1} \cdot day^{-1}$, GW drag (resolved and parameterized in the model) is contoured in blue for westward forcing and red for eastward forcing.

3.1 Formation of a Double-Maxima Wind Structure

The formation of a double-maxima wind configuration between 25 and 31 December was investigated by examining the PW and GW forcings on the background wind. **Figure 3** illustrates PW forcing (for wavenumbers 1-6) during 31 December for both model and observations. The mesospheric zero-wind line is notably lower in the model than in observations, revealing a zonal wind bias in WACCM-SD up to 7 $m\ s^{-1}$ above 0.1 hPa (Rüfenacht et al., 2018). Centered near 35°N and 80 km, the EP flux convergence of PWs indicates strong wind deceleration (blue contours) in excess of 60 $m \cdot s^{-1} \cdot day^{-1}$ in WACCM-SD. The observations reveal a similar PW forcing, albeit weaker and at a slightly lower altitude. In either case, the decelerative wave forcing occurs between the subtropical and polar jet cores. Following the EP flux vectors, this flux convergence region mainly results from the dampening of PWs propagating from the troposphere.

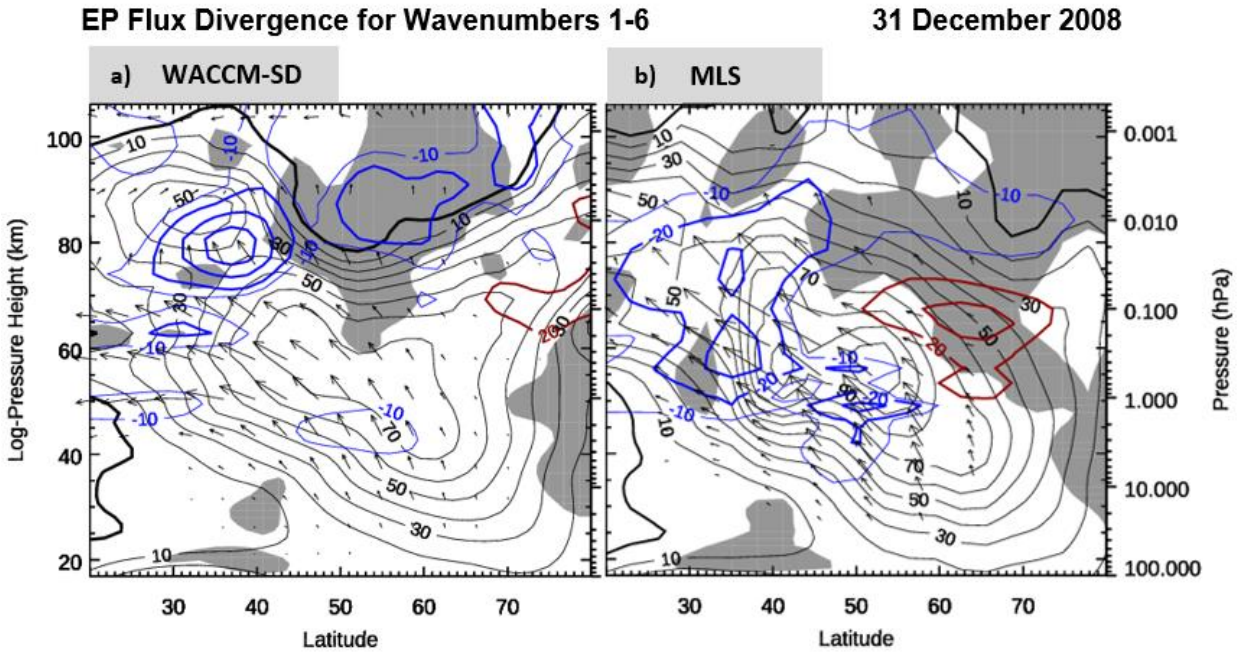

Figure 3. Altitude vs. latitude sections of PW EP flux for (a) WACCM-SD and (b) MLS data during 31 December 2008. Negative and positive EP flux divergence values are contoured every 20 $m \cdot s^{-1} \cdot day^{-1}$ in thick blue and red lines, respectively. Indicating the 10 $m \cdot s^{-1} \cdot day^{-1}$ isopleth, the thin blue contour illustrates the broad extent of PW forcing. The meridional EP Flux vector component was scaled by $(100\pi R_e \rho)^{-1} \cos\phi$ and the vertical component by $(R_e \rho)^{-1} \cos\phi$. The westward (dotted black contour) and eastward (solid thin black contour) $\bar{u}$ is contoured every 10 $m \cdot s^{-1}$, with the zero-wind line thickened. The grey-shaded regions represent areas of negative $\bar{q}_\phi$.

Wintertime PWs propagating upward from the troposphere can break along the edge of the polar vortex, as suggested by the EP flux pattern of Figure 3. The breaking process decelerates the equatorward flank of the polar night jet below 70 km. Subsequently, this weakened eastward wind allows eastward GWs to reach the mesosphere and impose an eastward GWD near the subtropical mesospheric jet core, shown in Figure 2d. Additionally, the presence of PW perturbations would introduce longitudinal variability in stratospheric wind field, allowing for the asymmetric upward GW transmittance.

While other studies have developed algorithms to estimate GWD with satellite data (Ern et al., 2004), we rely only on WACCM-SD to illuminate GW forcing. The total zonal GWD is determined by summing the parameterized and resolved GWD; the resolved GWD was estimated as the zonal EP flux divergence for waves of zonal wavenumbers greater than 6 (e.g., Fetzer & Gille, 1994). Nevertheless, we may indirectly assess GWD against observations by comparing diagnostic quantities affected by GWs, such as upwelling (positive $\bar{w}^*$), Brünt-Väisälä frequency (N_B^2), and $\bar{q}_\phi$ (as shown in Figure 4). Near 80 km and equatorward of 30°N on 31 December, the eastward GWD (red contours in Figure 2d) is significantly stronger than the westward PW forcing (Figure 3a). Thus, the net wave forcing (from GWs and PWs) is eastward which helps to maintain the subtropical mesospheric jet core while driving an equatorward meridional circulation. The adjacent westward GWD on the poleward side also dominates the net wave forcing. By the end of December (Figure 2d), GWD became increasingly westward in the mid-

latitudes (with values exceeding 60 $m \cdot s^{-1} \cdot day^{-1}$) and concentrated near the zero-wind line. This led to the wind shear increase evidenced by the constricted isotachs. The pronounced net westward forcing would drive a poleward meridional circulation between 40°-50°N. By continuity, we would expect enhanced upwelling around 30°-40°N just below ~80 km.

Figure 4a shows the time-latitude evolution of GWD averaged between 0.2 hPa and 0.02 hPa, where strong GWD appears in Figures 2c and 2d. The formation of the double-maxima wind structure on 31 December (vertical dashed line) occurs with the poleward movement of the polar jet as represented by the dashed black contours. A strong westward GWD (blue regions) persisted over the polar jet and followed its migration north. Eastward GWD began to dominate the subtropics due to weakened underlying winds due to PW dampening noted in Figure 3. With the SSW onset (vertical solid line), GWD eventually became eastward throughout NH due to the underlying stratospheric wind reversal (De Wit et al., 2014). Figure 4b illustrates the corresponding PW forcing in WACCM-SD at the same altitude range. Around 31 December, the peak in westward PW acceleration between 30°N and 40°N corresponded with the formation of the double maxima and is located between the subtropical (solid black contours) jet and the slightly lower polar jet (dashed black contours). Comparing Figures 2d and 3a, peaks in eastward GWD dominated PW forcing equatorward of 40°N near 0.02 hPa, locally accelerating the subtropical jet. Regardless, the position and strength of westward PW acceleration between the subtropical and polar jets in Figures 3a and 4b suggests that PWs are the driving mechanism for the double-maxima wind configuration. The reason for PW deposition in this location may be illuminated by further examining the background conditions.

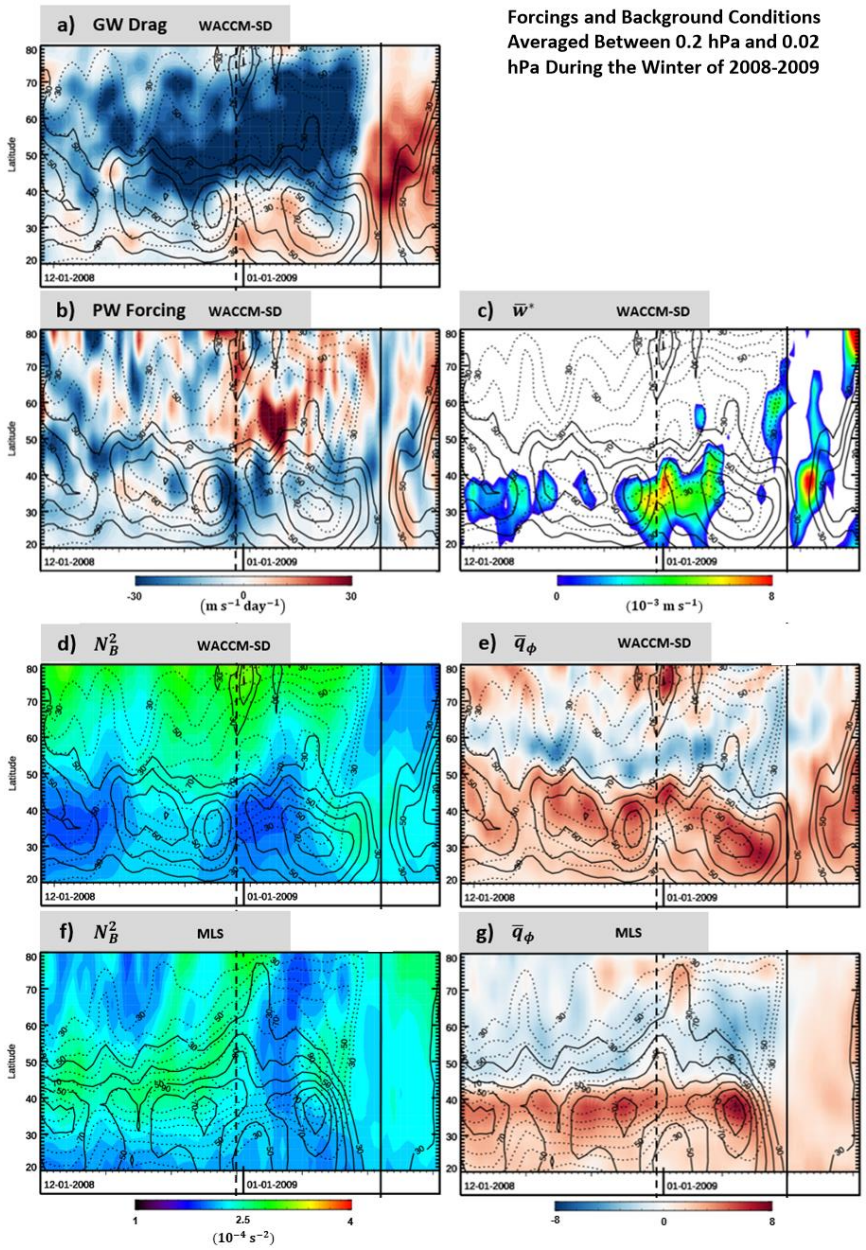

Figure 4. Latitude-time sections from (a-e) WACCM-SD and (f-g) MLS averaged between 0.2 hPa and 0.02 hPa showing (a) GW drag, (b) PW acceleration, (c) upwelling or positive $\bar{w}^*$, (d, f) N_B^2, and (e, g) nondimensionalized $\bar{q}_\phi$. The $\bar{u}$ values averaged from 1.0 to 0.1 hPa indicates the polar jet (dashed contours). The $\bar{u}$ values averaged from 0.1 to 0.01 hPa indicates the subtropical jet (solid contours). Vertical dashed line marks the formation of a double-maxima structure on 31 December 2008. Solid vertical line marks SSW onset on 22 January 2009.

The enhanced upwelling expected around 31 December between 30°-40°N is seen in Figure 4c. The enhanced upwelling adiabatically cooled the subtropics, leading to a decrease in the vertical temperature gradient. This is evidenced by the corresponding decrease N_B^2 over the subtropics in both the model and observations (Figures 4d and 4f). For WACCM-SD, **Figures 5**a and 5b show the meridional structure of N_B^2 for 25 and 31 December. Over this time span, the

diminished N_B^2 region (in blue) between 70-80 km extended northward and became situated between double-maxima wind structure. The effect of adiabatic cooling on the stability of the atmosphere was investigated through $\bar{q}_\phi$ in Figures 4e and 4g. Generally, the sign changes in $\bar{q}_\phi$ occur at approximately 45°N and 65°N. With the double-maxima wind formation, $\bar{q}_\phi$ at high latitudes increases with the acceleration of the mesospheric wind (solid black contours). In WACCM-SD, the mesospheric zonal winds show high- and low-latitude maxima resembling a configuration conducive to instability between the latitudes of 45°N and 65°N (e.g., Orsolini & Simon, 1995).

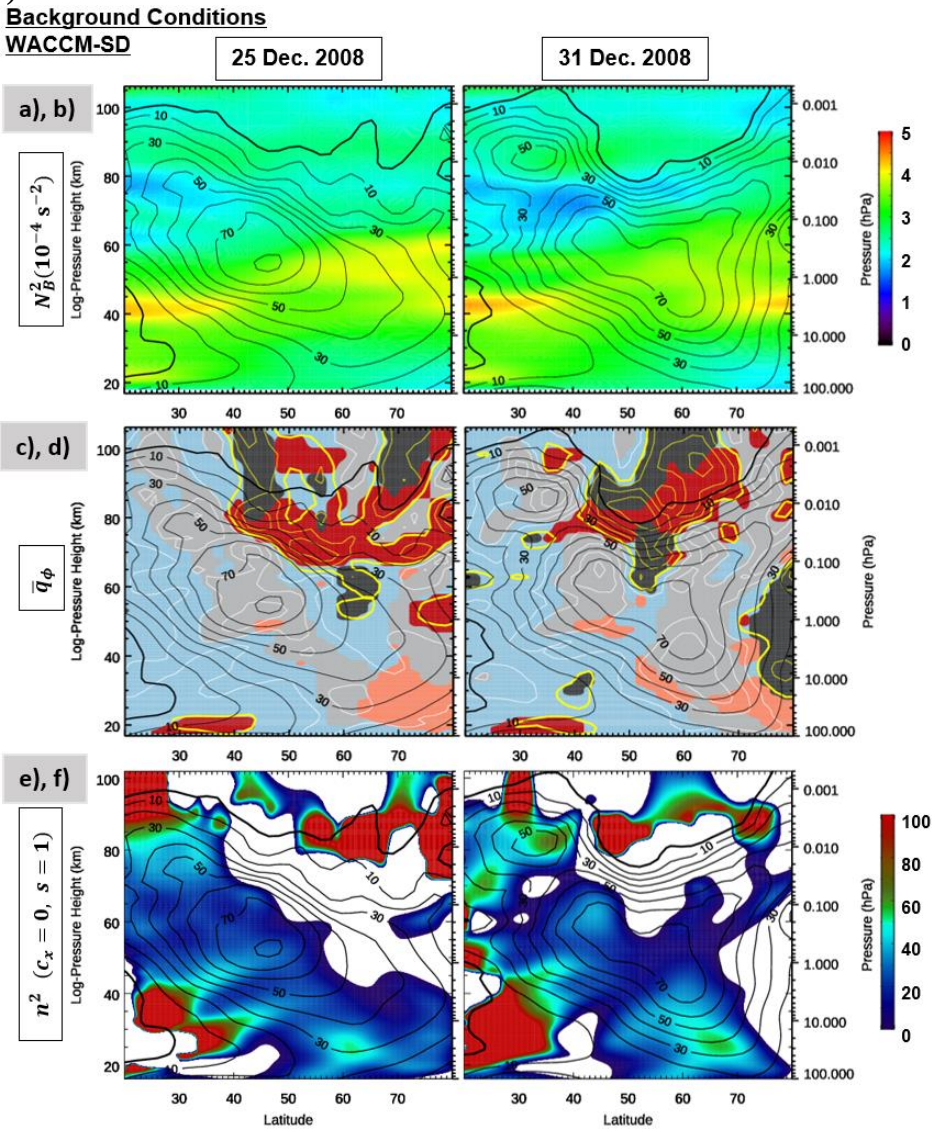

Figure 5. Altitude vs. latitude sections of (a, b) N_B^2, (c,d) nondimensionalized $\bar{q}_\phi$, and (e,f) nondimensionalized n^2 in WACCM-SD for 25 December 2008 (left column) and 31 December 2008 (right column). (c, d) White and yellow contours (every 1 unit) indicate positive and negative $\bar{q}_\phi$ respectively with the bold yellow contour indicating the zero value. In reference to the RHS of Equation 1, blue-, grey-, and red-shaded regions indicate the dominance of the first, second, and third term, respectively. Dark (light) colors represent a negative (positive)

contribution to $\bar{q}_\phi$. Eastward $\bar{u}$ is contoured every 10 m·s^{-1} as thin black contours, with the zero-wind line thickened.

Figures 5c and 5d illustrate the nondimensionalized $\bar{q}_\phi$ and the relative dominance of each RHS term in Equation 1. The positive and negative $\bar{q}_\phi$ values are contoured in white and yellow, respectively. The negative $\bar{q}_\phi$ region is bounded by a bold yellow contour. Regions where the magnitude of the beta term, barotropic term, and baroclinic term (RHS terms in Equation 1) dominate are shown by the blue, grey, and red shading, respectively. Light and dark tints of each color indicate whether the term is contributing positively (light) or negatively (dark) to $\bar{q}_\phi$. For example, since the planetary vorticity term is positive definite, the dominance of this term is always represented as a light blue. With the development of the double-maxima wind structure, positive $\bar{q}_\phi$ values developed well-organized cores (white contours), nearly collocated with the local wind maxima. These enhanced values were dominated by the barotropic term (grey region), reflecting the strong horizontal wind curvature and the tightening of the isotachs. This enhanced wind shear was due to the strong westward GWD near the zero-wind line and the adjacent eastward GWD (see Figure 2d). By the end of December, a valley of low $\bar{q}_\phi$ developed between the local maxima extending diagonally from the poleward side of subtropical jet near 80 km, across to a negative pocket at 75 km and 30°N, and down to equatorward side of the polar jet near 60 km. This valley between the local wind maxima was dominated by the baroclinic term (shaded in dark red).

Equation 1 indicates that $\bar{q}_\phi$ depends also on N_B^2 through the baroclinic term. Assuming other variables being fixed, a decrease in N_B^2 would diminish $\bar{q}_\phi$. In comparing Figures 5a and 5b, strong vertical wind shear (evidenced by the tightened isotachs) coincides with a drastic decline in N_B^2. The decline in N_B^2 also coincides with the extension of the negative baroclinic component (3rd term in Equation 1 that is dependent on N_B^2) in $\bar{q}_\phi$ into the subtropical mesosphere. Therefore, the development of a double-maxima wind structure development led to the lowered N_B^2 distribution and diminished $\bar{q}_\phi$values.

Furthermore, Equation 2 indicates that decreasing both N_B^2 and $\bar{q}_\phi$ would reduce the squared refractive index (n^2) in the subtropics. For PWs propagating westward relative to the flow, the reduction in refractive index can impact PW propagation and, ultimately, where PWs deposit their energy upon dissipation. Figures 5e and 5f show the n^2 evolution for stationary PW of zonal wavenumber 1. On 31 December, the aforementioned valley of low $\bar{q}_\phi$ (due to increased wind shear) reduced n^2 and created pockets of wave evanescence (i.e., negative n^2). Moreover, the enhanced (and positive) $\bar{q}_\phi$ seen in Figures 5c and 5d manifested as localized regions of large n^2.

Taken together, these changes in n^2 suggest a waveguide development that encourages PWs to propagate toward the intervening region between the subtropical and polar jets (due to enhanced n^2 at 44°N and 60 km). The negative n^2 pockets and diminished n^2 areas between the jet cores (roughly 30-40°N and 60-80 km) likewise limit PWs from further propagation. This is supported by the strong PW EP flux convergence shown in Figure 3a. To this end, a positive feedback loop was created promoting the separation of the jet cores. Increased PW forcing assisted in upwelling (along with GWD). PW propagation was modulated by the enhanced upwelling resulting in greater localized PW forcing. The increased wave forcing around the jet

cores also enhanced the vertical and horizontal curvature of the zonal winds and generated a more unstable flow (evidenced by growing evanescent regions in Figures 5e and 5f).

Figure 6 illustrates the distribution of carbon monoxide (CO) which serves as a nearly conservative tracer to illuminate the horizontal flow evolution (e.g., Solomon et al., 1985). As discussed earlier, the juxtaposition of the evanescent and high n^2 region at 0.2 hPa in Figure 5f creates an ideal zone for PW dissipation. On 31 December (Figure 6a), a wavenumber-1 perturbation appeared as a low-pressure region (evidenced by black geopotential height contours) equatorward, increasing the zonal wind (white contours) near the International Date Line. This distorted pattern helped form the subtropical mesospheric jet seen in Figures 2d and 3a. By 6 January (Figures 6b), the vortex further deformed with features indicative of PW wave breaking; A filament of low CO (high potential vorticity) air was advected equatorward around 30°N, just poleward of the subtropical jet. This filament structure fostered the local meridional gradient reversal of the potential vorticity, that destabilized the flow. Notably, this wavenumber-1 pattern prior to a split SSW suggests that the dominant wavenumber associated with the formation of a double-maxima configuration does not necessarily coincide with that of the SSW event.

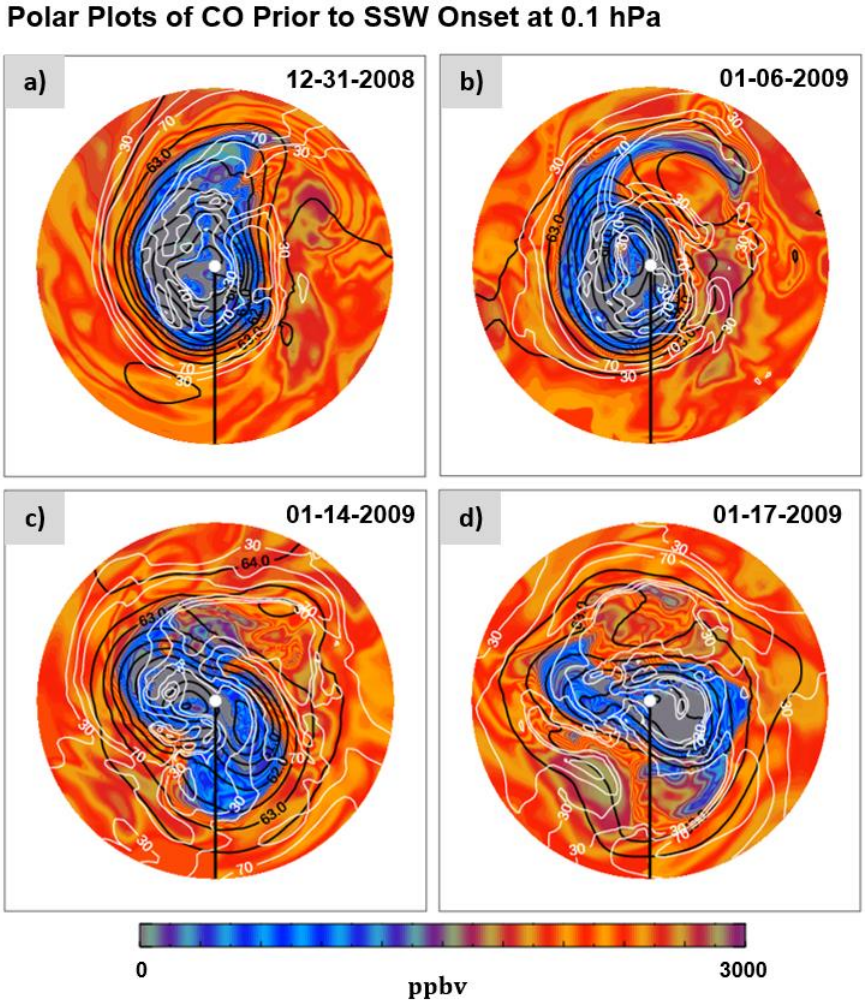

Figure 6. Stereographic polar projections of CO from WACCM-SD at 0.1 hPa. Geopotential height (black contours) is incremented by 0.5 km. Zonal wind isotachs of 30, 50,

and 70 $m \cdot s^{-1}$ are shown in white contours. The thick black vertical line depicts the Prime Meridian.

In summary for this case study, the interplay between GWD and PW forcing resulted in a double-maxima wind configuration. Both PWs and GWs deposited westward drag in the middle to high latitudes. The upward transmittance of GWs that imposed strong eastward drag on the subtropical mesosphere was ultimately modulated by underlying stratospheric winds due to PW forcing. These three factors enhanced subtropical upwelling, leading to changes in N_B^2 through adiabatic cooling. Thus, a positive feedback loop was created in which the double-maxima wind configuration was promoted, and the mesospheric flow became more susceptible to shear instability.

3.2 Emergence of EPWs and Instability

The development and persistence of the double-maxima wind structure prior to SSW encouraged the generation of instability waves leading up to SSW onset. **Figure 6** shows the polar plot at 0.1 hPa of carbon monoxide (CO) which serves as a long-lived tracer to illustrate the evolving dynamics. By mid-January (Figures 6c and 6d), low CO air (bluish color) was drawn towards the equator in a wavenumber-2 pattern as a result of two partially-separated low-pressure systems. Between 14 and 17 January, the wavenumber-2 GHP slowly propagated eastward. For both models and observations, **Figure 7** investigates the evolution of this pattern by showing the wavenumber-2 GHP amplitude (averaged between 45°N and 55°N) as a function of zonal phase speed and time. By the end of December, when the wind structure was in a double-maxima configuration (dashed vertical line), the wave's phase speed distribution shifted toward a mean eastward phase speed over a deep layer. The GHP amplitudes amplified simultaneously and diminished with altitude. About 10 days before SSW onset, the wave signatures peaked near 5 $m \cdot s^{-1}$ eastward phase speed. At 0.1 hPa, near the intervening level between the two jet cores (c.f., Figure 5), Figures 7c and 7f show a similar slow eastward propagation previously noted in the wavenumber-2 CO pattern of Figures 6c and 6d. After SSW onset, a strong westward PW2 signature coincides with stratospheric wind reversal. Notably, these westward-propagating PWs are instability waves that drive SSW recovery in the mesosphere and lower thermosphere (Limpasuvan et al., 2016). Overall, the structure and amplitude characteristics are remarkably similar between model and observations.

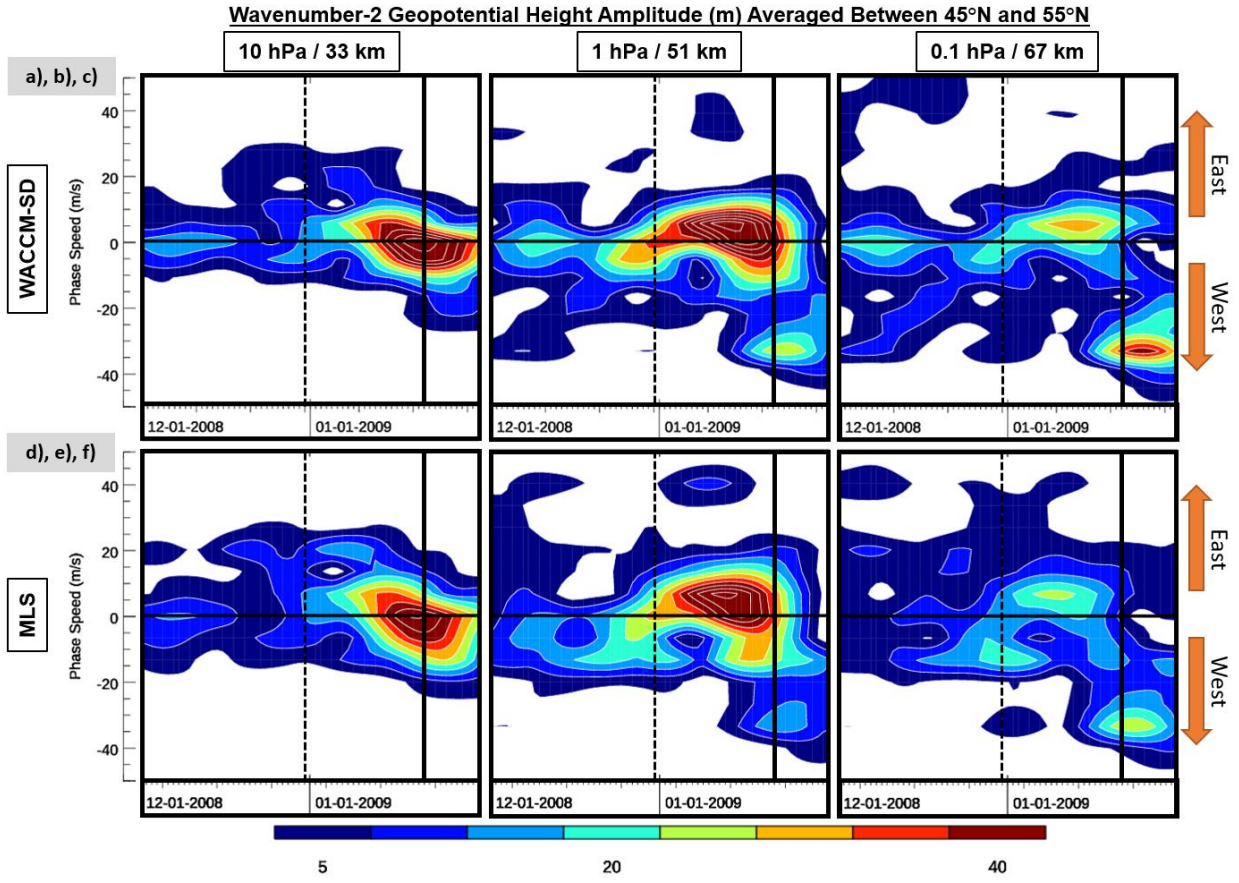

Figure 7. Zonal phase speed vs. time plot of wavenumber-2 GHP amplitude (m) at 67 km averaged between 45°N and 55°N. White contours increment by 5 $m \cdot s^{-1}$. Positive phase speed indicates eastward movement.

Figures 8a,b,d,e show the EP flux for wavenumber-1 and -2 PWs (PW1s and PW2s, respectively) of all phase speeds just prior to SSW onset (16 January 2009) in both the model (top row) and observations (bottom row). The observed and modeled double-maxima wind structure persisted from an earlier time in the winter (see Section 3.1). In both model and observations, an extensive region of negative $\bar{q}_\phi$ (grey-shaded area) appeared in a meridional local minimum of zonal-mean zonal wind near 0.1 hPa. The strong wind curvature responsible for a negative $\bar{q}_\phi$ is emphasized by the orange horizontal line in the Figures 8a and 8d crossing the same 30 $m \cdot s^{-1}$ isotach twice. Consistent with the split polar vortex, PW2s dominated the wave flux activity. The observed PW2 activity (Figure 8e) showed one broad EP flux divergence region above the polar stratosphere while the simulated PW2 activity (Figure 8b) revealed two separate regions on the poleward and equatorward side of the polar jet. Areas of EP flux convergence (blue contours) appear mainly above and on the equatorward side of the polar jet.

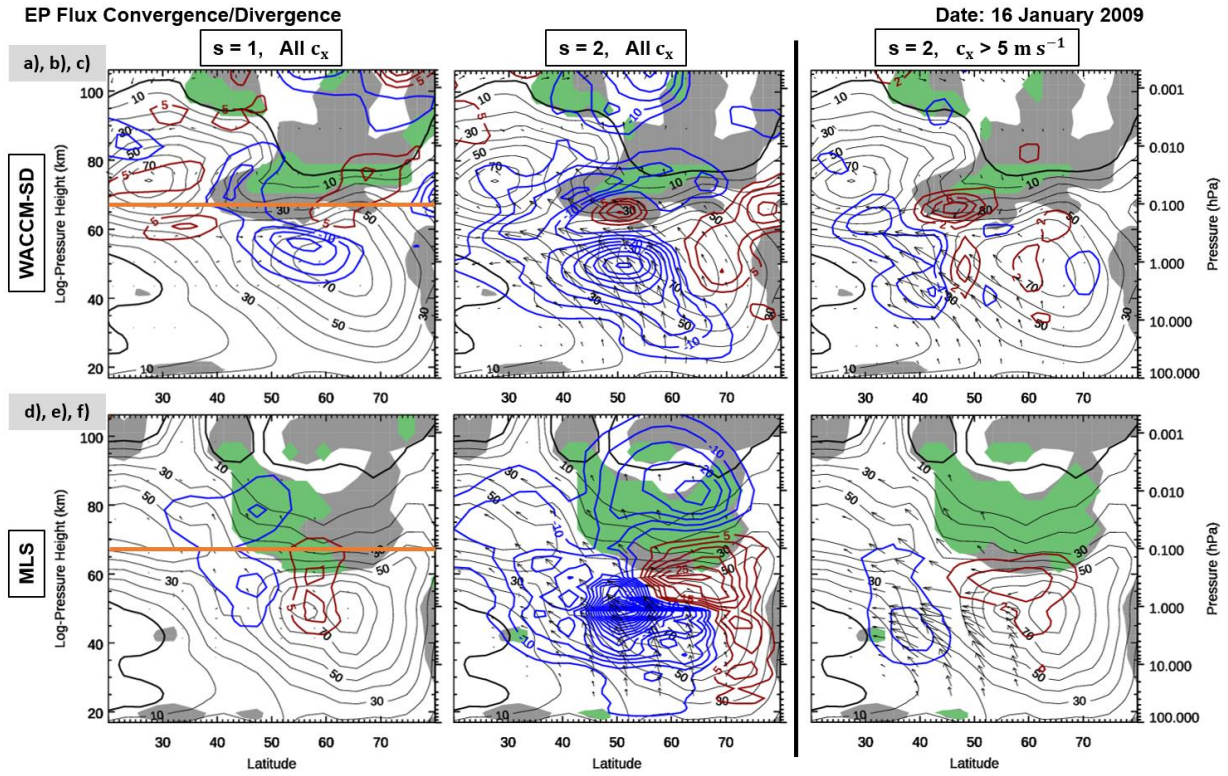

Figure 8. Altitude vs. latitude sections of PW1 (left column) and PW2 (middle column) for all phase speed, and for EPW2 (right column) as computed from WACCM-SD (top row) and MLS data (bottom row). Negative (blue) and positive (red) EP Flux divergence is contoured every 5 m·s^{-1}·day^{-1}), except for EPW2 where the contour interval is 2 m·s^{-1}·day^{-1}. Eastward $\bar{u}$ is contoured every 10 m·s^{-1} as thin black contours, with the zero-wind line thickened in solid black. The negative $\bar{q}_\phi$ region is grey-shaded. The presence of a critical layer inside the negative $\bar{q}_\phi$ regions is shaded in green. The EP Flux vector components are scaled as done in Figure 3, but the EPW2 vector magnitudes are multiplied by 10.0.

We then elucidate EPWs by band-pass filtering for wavenumer-1 and wavenumer-2 PWs with eastward phase speed of 5 m·s^{-1} and greater. This phase speed was selected based the identified PW2 eastward peak in Figure 7. Considering the broad phase speed distribution in Figure 7, the derived EPW fluxes are expected to be smaller than the total PW fluxes with all phase speeds. Nevertheless, filtering minimizes the influence from upward-propagating quasi-stationary PWs and better illustrate the propagation and forcing instability PWs. The resulting EPW2 EP flux structures are shown in Figures 8c and 8f. In addition to an apparent source below the stratosphere, the EPW2 activity emerged from the edges of the negative $\bar{q}_\phi$ region with an overlying critical layer (green shading). The EPW2 EP flux vectors emanate from regions of EPW2 EP flux divergence (red contours) and overlap with the mid-latitude region of PW2 flux divergence (Figures 8b and 8e). The EP flux divergence suggests the localized EPW2 wave growth from instability. This growth occurred in eastward flow regime which indicates that these instability waves will have an eastward phase speed, as supported by the eastward shift in the phase speed distribution in Figure 7 around 16 January. The emanating EPW2 flux activity pointed equatorward toward a flux convergence region in the subtropics. Overall, the characteristics of these instability waves are consistent with wavenumber-2 eastward PWs identified by Coy et al. (2011) and Iida et al. (2014).

3.3 Instability Waves from an Over-reflection Perspective

Figure 9 illustrates the altitude-time evolution of the vertical component of PW EP flux (upward in brown contours and downward in teal contours) and EP flux divergence (red contours) averaged between 45°N-55°N for WACCM-SD (Figures 9a,b,c,d) and 55°N to 70°N for MLS (Figures 9e and 9f). As noted by Coy et al. (2011), bursts of PW2 signal originating near the surface reached the 1-hPa level within days to weeks. Notably, WACCM-SD data shows consistently stronger vertical fluxes than MLS above 0.1 hPa and may account for the model wind bias at this higher altitude range.

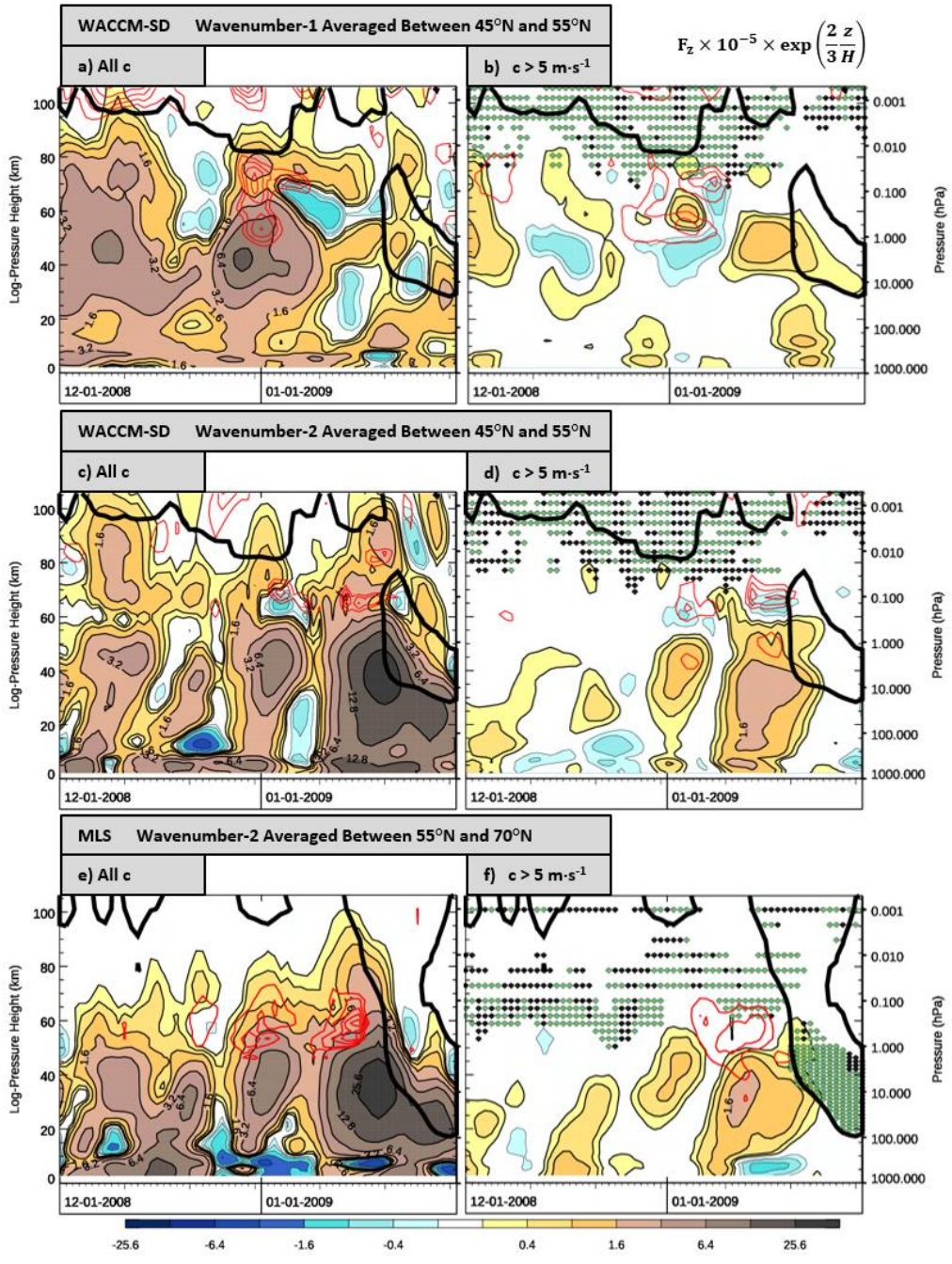

Figure 9. Altitude vs. time showing vertical EP flux (filled-contours) of wavenumber-2 disturbances for waves of (a, c) all phase speeds and (b, d) eastward phase speeds greater than 5 $m \cdot s^{-1}$. Regular-sized (thin) black contours of +(-) 0.2×2^m $kg \cdot s^{-2}$, $m \in [1,2,3,4,5,6,7,8]$ outline upward (downward) fluxes. Red contours show EP flux divergence and are incremented by (a, c) 5 $m \cdot s^{-1} \cdot day^{-1}$ and (b, d) 2 $m \cdot s^{-1} \cdot day^{-1}$. Thick black contour depicts the zero-wind line. Stippled regions shown in b and d also apply to a and c, respectively. Locations with negative $\bar{q}_\phi$ are marked by black stipples. Locations where a critical layer exists inside a region of negative $\bar{q}_\phi$ are marked by green stipples. Data sources and latitudinal averages are labeled at the top of each plot.

In Figures 9a,c,e, PWs exerted persistent eastward forcing (red contours) near 0.1 hPa around early and mid-January, coinciding with the incidental bursts of the underlying wave activity, also seen in Figures 8b and 8e. A burst of upward PW1 flux (Figure 9a) coincided with the formation of a double-maxima wind structure on 31 December. A deep layer (1.0 hPa to 0.02 hPa) of PW growth, coinciding with a decrease vertical EP flux suggests PW1 instability. This formation of a PW1 eddy pattern was noted in Figures 6a and 6b at the same height. Figure 9b suggests that this instability results in some over-reflection as downward EPW1 EP flux (blue contours) is seen roughly below from a region of EPW1 divergence. Therefore, the double-maxima wind structure was ultimately created from the growth of a PW1 unstable mode.

Filtered for eastward phase speed greater than 5 $m \cdot s^{-1}$, Figures 9b and 9d show that EPW2 fluxes comprise some of the upward burst of PW2 but tend to be much weaker than the PW2. This is to be expected since the total PW2 has a broad range of phase speeds as suggested in Figure 7. After the formation of a double-maxima wind configuration, occurrences of PW2 growth in the mesosphere (shown by EP flux divergence in Figures 9c and 9e) were evident suggesting instability. The eastward component of PW2 EP flux divergence (shown in Figures 9d and 9f red contours) occurred below a critical layer that laid within a negative $\bar{q}_\phi$ region (green stipples).

This configuration suggests EPW2 growth from over-reflection. This was particularly evident in the model (Figure 8c) as downward-pointing vectors emanated from a region of EPW2 divergence. These downward-pointing vectors were not as evident in observations (Figure 8f), although the EPW2 group velocity was sharply diverted equatorward. Over-reflection is particularly evident in Figures 9c and 9d by the downward EP flux (blue areas) emanating from the region of wave growth at the beginning of January. The downward flux produced by other divergence regions may not be as evident as they may be masked by strong upward flux from tropospheric sources. The downward flux may also partially negate the upward flux, resulting in valleys between upward flux extrema.

As illustrated in Figure 1, instability wave can manifest as over-reflection and over-transmission as suggested by studies like Lindzen (1980) and Harnik & Heifetz (2007). Our study will regard the over-reflected and over-transmitted wave as the downward-propagating and upward-propagating component of the instability wave, respectively. However, unlike the idealized scenario, the over-reflected and over-transmitted waves have both vertical and meridional components in their group velocity (e.g., Figure 8).

This is expected since the negative $\bar{q}_\phi$ region consists of the relative contributions from the baroclinic and barotropic terms (in Equation 1), and these contributions vary in time as shown in Figures 5c and 5d during late December with the formation of the double-maxima wind

configuration. Thereafter, the negative $\bar{q}_\phi$ region (as shown in **Figure 10** within the yellow contours) became dominated by the baroclinic term (dark red) above the polar jet and the barotropic term (dark grey) on the poleward side of the subtropical jet. Above the polar jet, the dominance of the baroclinic term at high-latitudes would support a more vertical over-reflection while the dominance of the barotropic term at mid-latitudes (in the intervening region between the two jet cores) would support a more horizontal over-reflection. This mixing of baroclinic and barotropic contributions in the negative $\bar{q}_\phi$ region makes it difficult to identify instability waves simply from time-altitude sections (like Figure 9) if the instability EPW2 activity also propagate meridionally from the unstable region, as seen in Figures 8c and 8f.

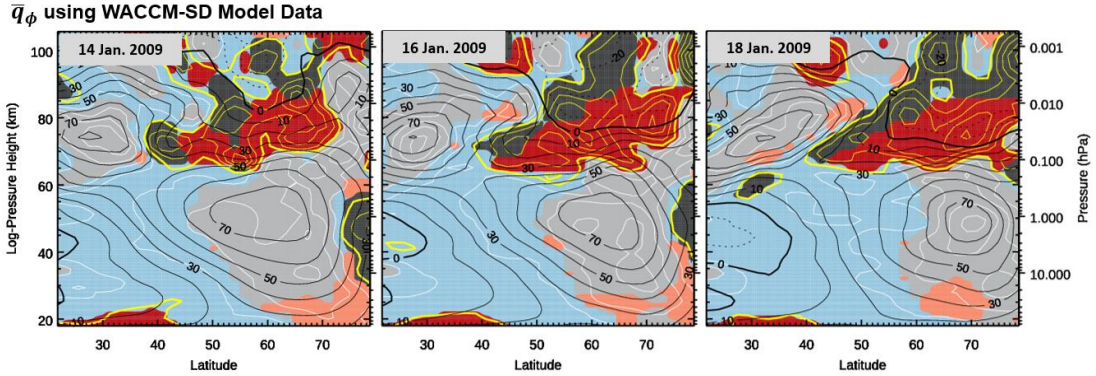

Figure 10. Altitude vs. latitude sections of nondimensionalized $\bar{q}_\phi$. Plotting convention is like Figures 5c and 5d except at different times. Eastward $\bar{u}$ is contoured every 10 m·s^{-1} as thin black contours, with the zero-wind line thickened.

Figure 10 shows that the two jet cores separated further as the polar jet migrated toward higher latitudes. This migration increased the meridional curvature of the zonal wind and thus increased $\bar{q}_\phi$ as evident by the maxima of white contours in Figure 10d at 1 hPa and 70°N. The increased $\bar{q}_\phi$ should coincide with an increase in the index of refraction (squared) n^2as defined in Equation 2. **Figure 11** examines n^2 that supports the linear propagation of EPWs and, for contrast, of stationary PWs. For EPWs, the eastward phase speed of 10 m·s^{-1} is used in the n^2 computation. Consistent with the latitude band selected in Figures 9a-d, the reference latitude used in Equation 2 is 50°N. White areas represent wave evanescent regions with negative n^2 values. Generally, the red regions correspond to extremely large n^2 values (>100), often occurring near critical layers.

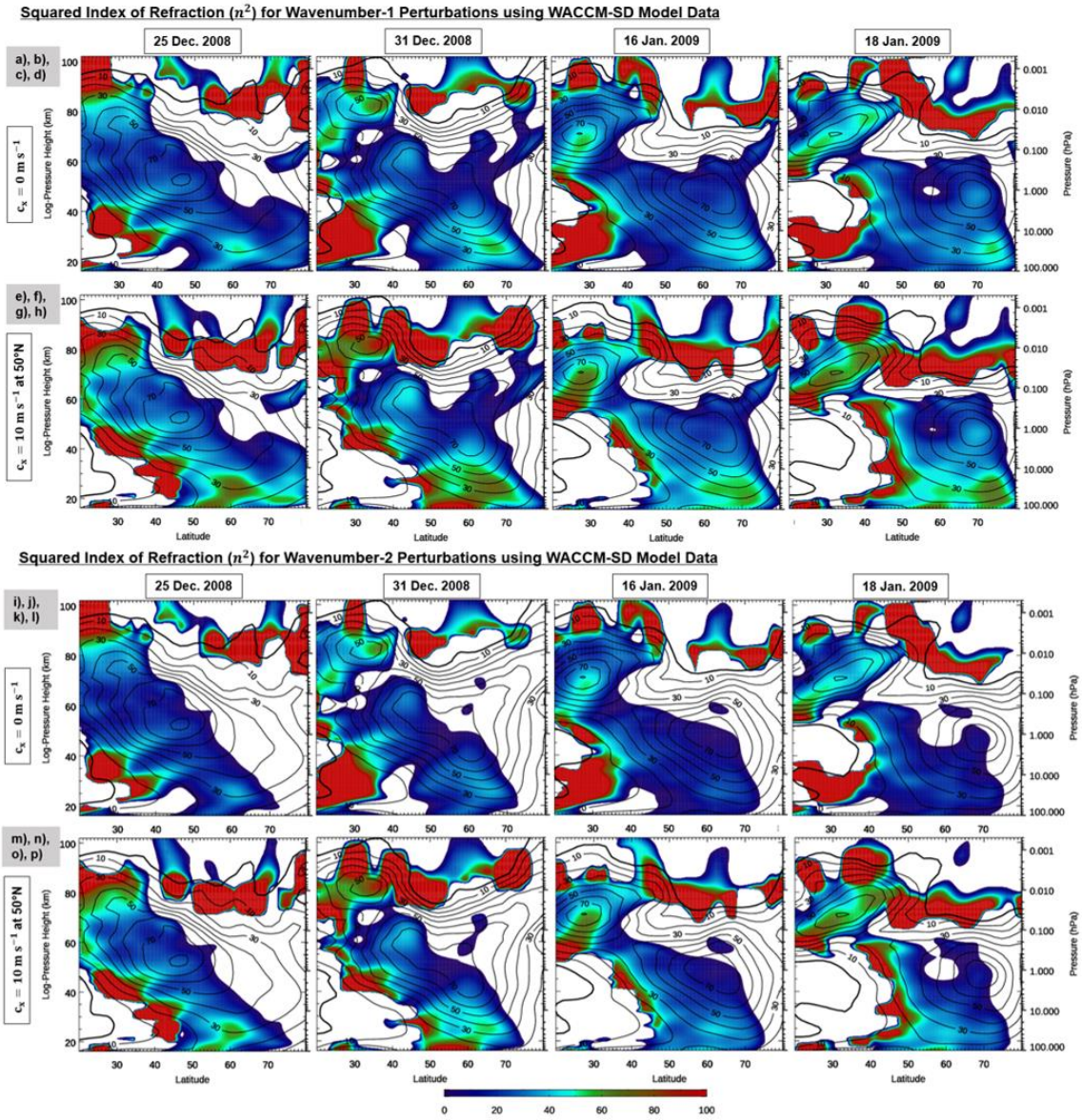

Figure 11. Squared refractive index, n^2 (color-filled contours) for PW1s (top) and PW2s (bottom) using WACCM-SD. For each row, PWs are specified by frequency and labeled in terms of phase speed (at a latitude if necessary) at the left of each row. Columns are organized by reference date. Eastward $\bar{u}$ is contoured every 10 m·s^{-1} as thin black contours, with the zero-wind line thickened.

Significant change in n^2 occurred between 25 and 31 December that promotes the separation of the subtropical and polar jets through local PW dissipation. With the polar jet migrating northward thereafter, n^2became more enhanced at higher winter latitudes throughout the stratosphere. This enhancement conditioned the background flow to guide PWs (originating in the mid-latitude troposphere) as well as EPWs more vertically near the edge of the polar vortex. Hence, a broad spectrum of PWs propagating from the lower stratosphere were more likely to reach the lower boundary of negative $\bar{q}_\phi$ (i.e., the turning level in Figure 1) and over-reflect. This likelihood is also seen in Figure 9 with the upward EP flux extending to higher altitude the double-maxima wind formation on 31 December. The vertical orientation of PWs

prior to SSW onset is common (e.g., Limpasuvan et al., 2012) and thus could explain why the appearance of EPWs have been noted, in particular, prior to SSWs as seen in Figure 9 (L. Coy et al., 2011; Iida et al., 2014).

Following the PW propagational path, the critical layer is absorptive if n^2 is positive approaching a critical layer. This is seen commonly on the subtropical side of the polar jet. If n^2 is negative approaching the critical layer, then the critical layer would cap an evanescent region (like in Figure 1). In reference to Figure 1, over-transmitted waves would be actualized in the positive n^2 region above the critical layer, which is roughly 20 km thick for all plots in Figure 11. Over-transmitted waves propagating from the critical layer can readily deposit their momentum creating a region of EP flux convergence (westward acceleration). This pattern is evident in Figure 8b and 8e as a region of PW2 EP flux divergence (red contours) juxtaposes with a region of EP flux convergence aloft (blue contours). When compared to n^2 for slow eastward waves on 16 January in Figure 11o, EP flux divergence occurred in the evanescent region while EP flux convergence occurred in a thin layer of positive n^2 aloft. As a result, the mesospheric zero-wind line descended (compare Figure 11o and 11p). The over-transmitted wave is not as evident for EPW2 on 16 January. However a small EP flux convergence near 0.002 hPa and 45°N in the model (Figure 8c) and EP flux vectors emanating toward the same region in the observations (Figure 8f) suggest that the over-transmitted wave may deposit further equatorward near the subtropical jet. This is further investigated through a composite study in Section 4. For both wavenumber-1 and -2, the evanescent region becomes thinner approaching SSW onset. We note that the vertical geometry for instability idealized in Figure 1 is homomorphic with the meridional geometry (Lindzen, 1988). While the vertical geometry is the most evident in Figure 11, a similar meridional-oriented geometry could also encourage over-reflection.

In addition to suggesting the occurrence of over-reflection/over-transmission by EPW2, Figure 11 addresses why instability waves have a mean eastward phase speed. Assuming the upward-propagating PW signal with a distribution of phase speeds, the EPWs would experience a critical layer above the polar jet that is lower in altitude (see Equation 2). As a result, EPWs encounter a thinner evanescent layer giving them a greater capability to tunnel (given a large enough amplitude) and, consequentially, over-reflect as well as over-transmit.

3.4 Recap of the January 2009 SSW Case

In summary for this case study, the interplay between GWD and PW forcing resulted in a double-maxima wind configuration. Both PWs and GWs deposited westward drag in the middle to high latitudes. The upward transmittance of GWs that imposed strong eastward drag on the subtropical mesosphere was ultimately modulated by underlying stratospheric winds due to PW forcing. These three factors enhanced subtropical upwelling, leading to changes in N_B^2 through adiabatic cooling. Thus, a positive feedback loop was created in which the double-maxima wind configuration was promoted, and the mesospheric flow became more susceptible to shear instability.

The mesospheric EPWs reported by Coy et al. (2011) and Iida et al. (2014) prior to the January 2009 SSW appear to be manifestations of shear instability. Mesospheric PW2 growth occurred multiple times throughout the 2008-2009 winter. Each occurrence of wave growth coincided with upward-propagating PWs reaching the lower boundary of the negative $\bar{q}_\phi$ region. By isolating waves with eastward phase speeds greater than 5 $m \cdot s^{-1}$, it is shown that most of the

local acceleration due to instability waves came at the expense of a westward acceleration in the subtropical stratosphere. Over-reflection appears in conjunction with these instability waves and is supported by configuration of critical and turning levels. The evanescent region between the critical and turning levels became thinner approaching SSW onset, making over-reflection and over-transmission more likely. Concomitant to over-reflection, tunneling would allow PWs to extend (and dissipate) aloft.

4 Composite of EPWs

A similar interplay between GWD and PW forcing is found prior to other SSWs as well (not shown). Thus, the evolution PW and GWD as well as the background wind are not unique to the often-studied January 2009 split SSW. Furthermore, after this double-maxima wind formation, instability EPWs were found to be associated with wavnumber-1 and wavenumber-2 perturbations prior to SSWs with either split and displaced vortices. While instability waves are not necessarily dependent on a double-maxima wind configuration, strong and persistent occurrences of these instability waves were found after the formation of a double-maxima and prior to SSW. In all cases, these EPWs significantly impact the wind structure of the middle atmosphere. In some cases, EPWs can produce enough local eastward acceleration to generate a tertiary local maximum between the polar and subtropical jets.

Composites of mesospheric EPWs prior to SSW events (listed in Table 1) were developed to elucidate the robust behavior of EPWs in the mesosphere prior to SSW onset. As in the case studies, EPWs were isolated to better understand the propagation of instability waves (since they have a mean eastward phase speed) while filtering out much of the other upward-propagating PW signature (albeit not all of it). Since wavenumber-1 and -2 instability waves do not necessarily occur in tandem, separate composites were created to distinguish PW1 growth events from PW2 growth events. A PW1 growth event was defined to occur when the EPW1 EP flux divergence exceeds a critical value of 10 $m \cdot s^{-1} \cdot day^{-1}$ in the upper extension of the polar eastward jet (roughly between 30°-80°N and 50-85 km) in close proximity to a negative $\bar{q}_{\phi}$ region and a critical layer. Since the wavenumber-2 growth signal tends to be weaker, a PW2 growth event was selected when the EPW2 EP flux divergence exceeded 5 $m \cdot s^{-1} \cdot day^{-1}$ in that same region. The reference date (i.e., Day 0) of the respective event marks when the criteria for a growth event is fulfilled. As seen in Figure 9, EP flux divergence from EPW1 (Figure 9b) and EPW2 (Figure 9d) growth are not mutually exclusive, occurring irrespective of each other.

In total, 11 cases for PW1 growth events and 8 cases for the PW2 growth events were found. The identified dates (in YYYYMMDD format) for Day 0 for the PW1 events are 19840206, 19841214, 19870102, 19890206, 19950115, 19971117, 20031206, 20051201, 20090110, 20111228, 20121219. The dates for the PW2 events are 19841202, 19840211, 19971212, 20031209, 20051223, 20090113, 20091229, 20121224. All growth events occur more than 8 days prior to an SSW onset. Given the broad phase speed range of associated with PW1 and PW2 (suggested in Figure 7), these growth events identify the localized EPW1 and EPW2 EP flux divergences suggestive of instability wave growth leading up to SSW onset. The composite was done after aligning each event on Day 0. As demonstrated in Figure 9d on 13 December 2009, a region of EP flux divergence develops within a matter of 1-2 days. A change in critical value (± 1-2 $m \cdot s^{-1} \cdot day^{-1}$) altered the Day 0 reference date of the PW growth event by roughly ±1-2 days. However, the composite results are largely unchanged.

637 **Figure 12** shows the meridional cross-sections of the composite EPW1 and EPW2 wave
638 activity, associated with the respective growth events. Well before the reference date (Day -35),
639 a local zonal-mean zonal wind maximum exists in the winter stratosphere defining the polar jet
640 core, similar to the climatology in Figure 2b. At this time, the EPW1 and EPW2 wave activities
641 are generally weak, especially for EPW2. Between Day -5 and Day 0, a double-maxima wind
642 structure develops (with a polar jet and subtropical jet). On Day -5, EPW1 and EPW2 activities
643 grow considerably with wave energy emanating from below, before being refracted toward the
644 subtropics near the stratopause. Some EPW1 activity continues to the top of the polar jet where
645 its flux convergence (blue contours) exerts westward forcing near the zero-wind line. By Day 0,
646 as expected from our composite criteria, we see a clear signature of wave growth. In particular,
647 the EPW1 flux divergence (red contours) exceeding 5 $m \cdot s^{-1} \cdot day^{-1}$ appears above the polar jet
648 core and adjacent to a relatively weaker flux convergence below. The EPW2 flux divergence
649 exceeding 2 $m \cdot s^{-1} \cdot day^{-1}$ appears above the polar jet core and flanked by areas of flux
650 convergence on the equatorward side. Thereafter, similar local eastward/westward forcing
651 pattern and wave activity continue to enhance as SSW onset approaches.

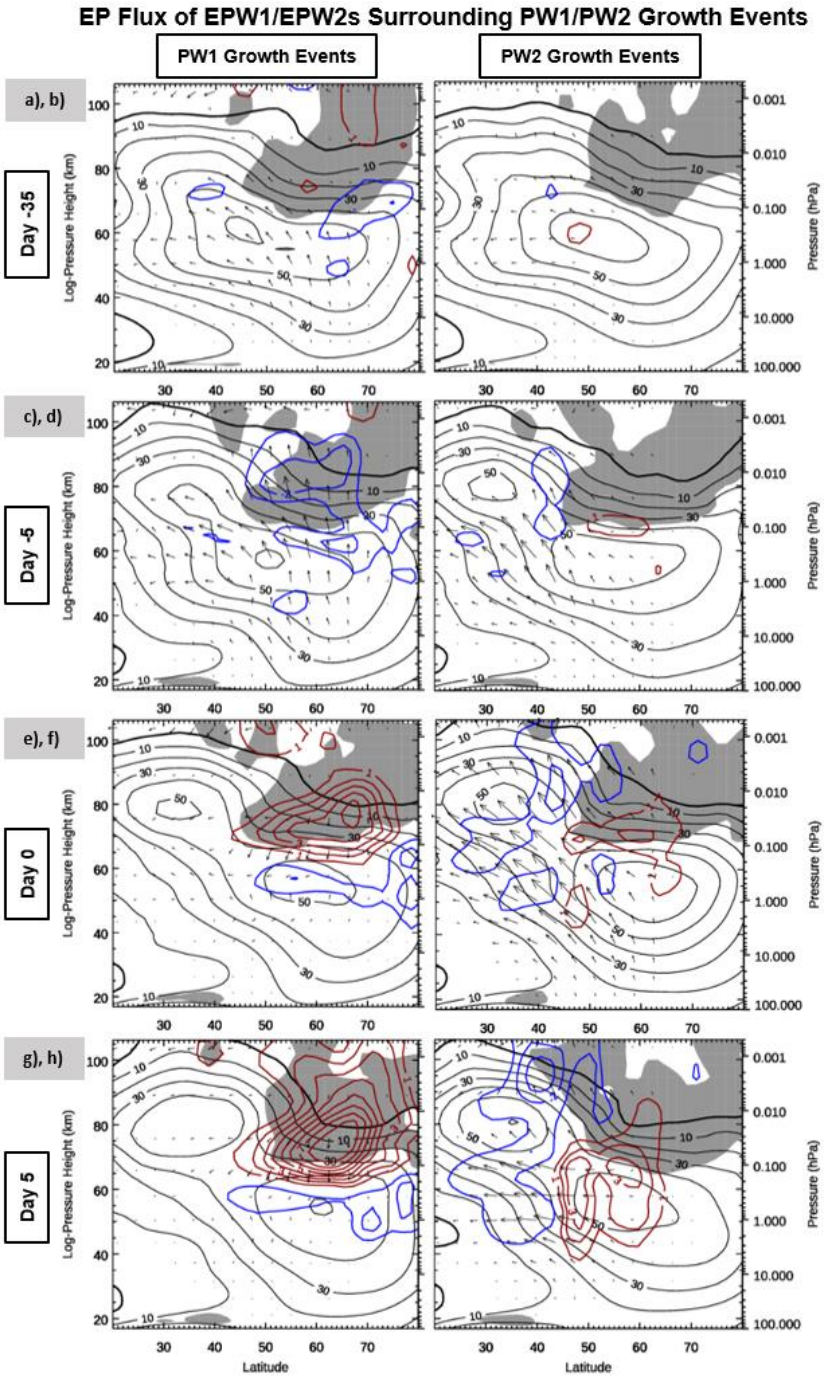

Figure 12. Altitude vs. latitude composites for (a, c, e, g) PW1 growth events and (b, d, f, h) PW2 growth events (right column) on days specified at the left of each row. EP flux convergence (blue) and divergence (red) contours increment by 1 $m \cdot s^{-1} \cdot day^{-1}$. The EP Flux vector components are scaled as done in Figure 3. Grey areas show regions of negative composited $\bar{q}_{\phi}$. Eastward $\bar{u}$ is contoured every 10 $m \cdot s^{-1}$ as thin black contours, with the zero-wind line thickened.

The features of EPW growth indicate a robust "source-and-sink" structure for instability waves and over-reflection that is different between EPW1s and EPW2s. During PW1 growth

events, EPW1s grow in the high-latitude mesosphere (with EP flux divergence accelerating the local flow) from an unstable region (grey shading) and emanate downward toward a region of EP flux convergence. This instability wave activity and associated forcings tend to reduce the vertical wind shear above the polar jet. On the other hand, EPW2s impose a more equatorward local eastward acceleration on the upper extension of the polar jet, peaking once above the polar jet and again in the intervening region between the two jet cores. Regardless, the development of these waves stabilizes the double-maxima wind structure. The direction of the EP flux vectors suggests that EPW2s (with a source above the polar jet) find their sink in the lower and poleward extension of the subtropical jet. Considering the effect of zonal wavenumber on n^2 illustrated in Figure 11, EPW1s would tend to propagate, and subsequently dissipate, further poleward than EPW2 (due to the second term in Equation 2).

While the EPW1 over-reflection is evident on Days 0 and 5, the EP flux convergence region associated with the accompanying over-transmitted wave is not evident. Large spatial variation in EPW1 over-transmission may account for the negligible flux convergence. For PW2 growth events, the EPW2 flux convergence region on the poleward side of the subtropical jet seems to indicate a more defined region for the dampening of over-transmitted waves.

The conditions leading up to these PW growth events were further investigated through **Figure 13**. The polar jet (dashed black contours) deviates farther poleward from the subtropical jet (solid black contours) approaching Day 0 (black vertical line) when the double-maxima wind configuration fully develops (Figures 12e and 12f). Illustrated in Figures 13a and 13b, the GWD pattern is similar to the 2009 SSW event (Figure 4a). During the double-maxima wind formation, westward GWD accompanies the underlying polar jet's migration into high latitudes while eastward GWD becomes dominant at lower latitudes. While not composited with respect to the SSW onset, the illustrated poleward spreading of GWD and its eventual sign switch in the mid- to high-latitude regions indicate an SSW onset roughly around days 10-20. Averaged between 0.1 and 0.01 hPa, the westward PW forcing becomes increasingly stronger between the polar and subtropical jets as they separate (Figures 12c and 12d). The westward PW forcing eventually maximizes and spreads throughout the winter hemisphere around SSW onset (days 10-20).

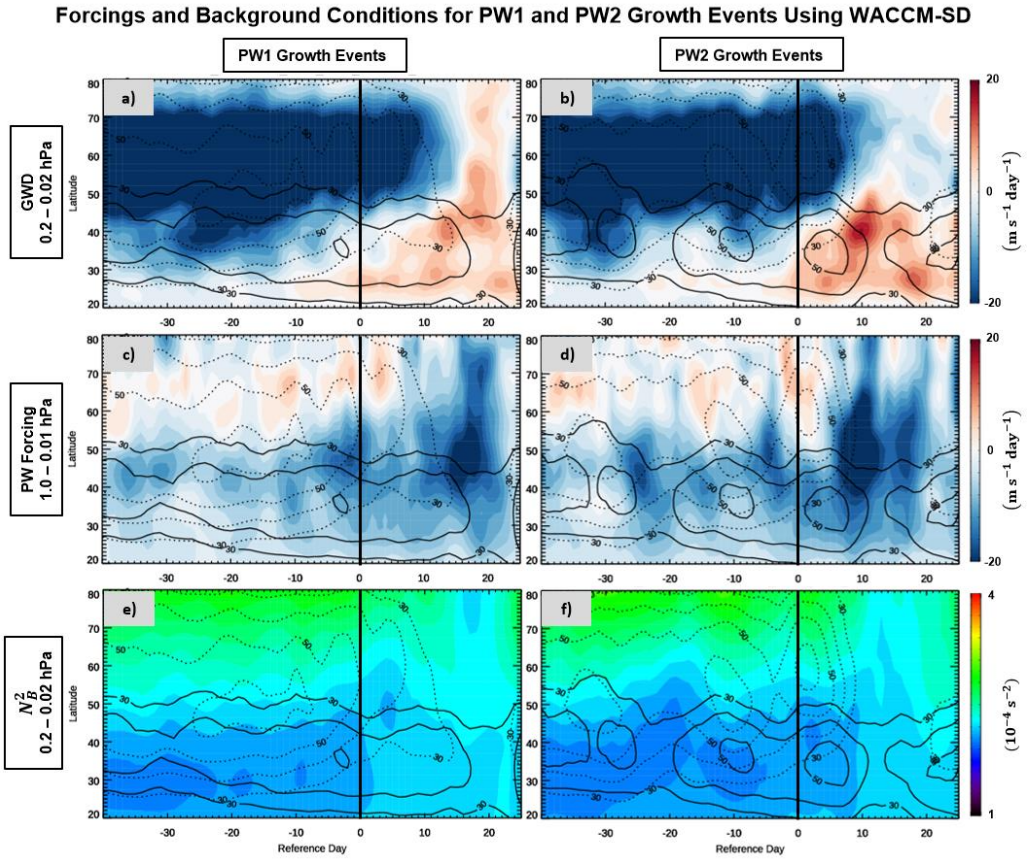

Figure 13. Latitude vs. time composites of (left column) PW1 and (right column) PW2 growth events showing. Variables and vertical averaging are indicated to the left of each row. GW drag is calculated by summing parameterized GW drags and EP flux of wavenumbers greater than 6. Zonal-mean zonal wind averaged from 1.0 to 0.1 hPa indicates the position and strength of the polar jet (dashed contours) and the zonal-mean zonal wind averaged from 0.1 to 0.01 hPa indicates the position and strength of the subtropical jet (solid contours).

Akin to the 2009 SSW case (Figure 4), the net eastward forcing in the subtropical regions would lead to localize upwelling and adiabatic cooling. These conditions accompany N_B^2 reduction (blue regions in Figures 13e and 13f) that eventually subside around days 10-20. For both PW1 and PW2 growth events, the low N_B^2 region in the subtropics migrate poleward with the polar jet and the PW dissipation. However, during the PW2 growth event, low values of N_B^2 migrate poleward twice over a period of ~15 days leading up to Day 0. These pulses of low N_B^2 migration coincide with pulses of strong zonal-mean zonal winds which may be unique to the development of EPW2.

Figure 14 shows n^2 for stationary and eastward PWs associated with the composited wind structure for the PW1 growth event (top plots) and PW2 growth event (bottom plots). While suggesting how the composited wind allows PW propagation, the illustration does not illuminate the average PW propagation of individual events and associated wind. Accordingly, the illustrated n^2 highlight the robust effect of a double-maxima wind configuration on PW propagation. Like Figure 11, the reference latitude for a phase speed is set such that the n^2 evaluates the propagation path of a PW that retains its zonal wavenumber by changing in zonal

711 phase speed with latitude. A 30 m·s^{-1} eastward phase speed is chosen to emphasize the difference
712 in the n^2 field for stationary and eastward PWs.

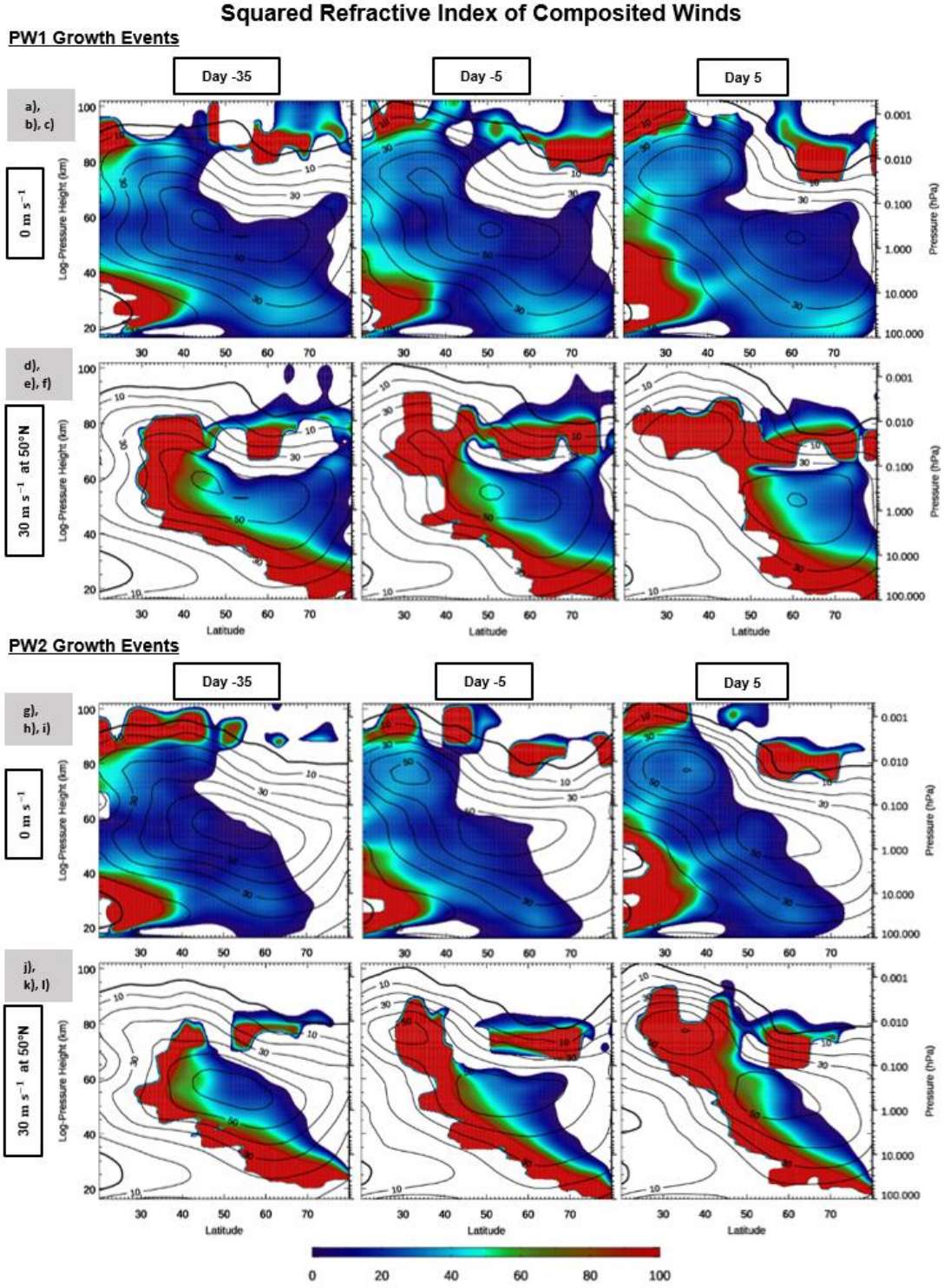

713
714 **Figure 14.** (a-f) PW1 and (g-l) PW2 growth event composite of the nondimensionalized
715 squared refractive index (filled contours). For each row, PWs are specified by frequency and
716 labeled in terms of phase speed (at a latitude if necessary) at the left of each row. Columns are

organized by reference date. Eastward $\bar{u}$ is contoured every 10 m·s^{-1} as thin black contours, with the zero-wind line thickened.

As suggested in Figure 13, the decrease in N_B^2 should lower n^2 and alter PW propagation. Comparing Day -35 to Day -5 in Figures 14a and 14b, n^2 decreases below the developing subtropical jet (around 60 km). For eastward PW1s (Figure 14e), n^2 turns negative here, creating an evanescent region and constricting the PW propagation path. For the PW2 growth event, the region of allowable PW propagation also shrinks. Overall, the composite shows the occurrence of the bottlenecking effect of n^2 between the newly formed polar jet and the subtropical jet that promote a region prone to PW deposition. Although not composited for the formation of a double-maxima wind structure, Figure 14 illustrates that the evolution of the background conditions that lead to shear instability appears consistent with the proposed mechanism separating the jets, as detailed for the 2009 SSW event (Section 3). In particular, two main regions of positive n^2 with opposite signs in $\bar{q}_\phi$ (see also Figure 12) are consistently present in mid- to upper-latitudes and separated by an evanescent region. Thus, a turning level is present with an evanescent region and critical layer aloft. These positive n^2 regions are well separated for stationary PWs poleward of 45°N by 10-20 km. However, the gap between these regions shrinks in time toward Day 0 when the PW flux divergence maximizes. Near the altitude of 70 km, the gap is smallest around 55°N for PW2s and around 70°N for PW1s. This suggests that instability wave growth is associated with a thinning of the evanescent region.

Furthermore, PWs of higher eastward phase speeds tend to encounter a lower critical layer and a thinner evanescent region (as seen also in Figure 11). This shows that the wintertime middle atmosphere tends to over-reflect PWs with eastward phase speeds by Day 0 and shortly thereafter. Based on the localized westward acceleration (blue regions) on Day 5, Figure 12 shows that over-reflection would increase the amount of deposition below the subtropical jet and at the pole. Since eastward waves can only exist in faster eastward background flows, they are more constrained in latitude and altitude than stationary and westward PWs. The westward accelerations by eastward-propagating instability waves would occur in regions where stationary and westward PWs can still propagate. Therefore, the eastward bias of the instability PWs allows them to be able to alter the propagation path for other PWs with more westward phase speeds.

5 Summary

This study examines the strong growth of the mesospheric EPWs prior to SSW events between 1980-2013. These events are associated with both split and displaced vortex. Previously, Coy et al. (2011) and Iida et al. (2014) reported their presence specifically for the 2009 SSW event with a split vortex. With eastward zonal phase speed of ~10 m s^{-1}, these EPWs are attributed to shear instability between the double-maxima eastward wind configuration, characterized by the subtropical mesospheric wind maximum and a polar stratospheric jet core. Such wind structure emerged from the interactions between GWD and PW forcing. Preceding the formation of this double-maxima wind configuration was the presence of subtropical eastward GWD adjacent to the mid- to high-latitude westward GWD in the mesosphere. This distinctive GWD pattern induced a subtropical upwelling that locally lowered N_B^2 and $\bar{q}_\phi$. The resultant change in n^2 further promoted the separation of the polar and subtropical jets by directing PW damping toward the intervening region between the wind maxima. Our study shows that the formation of double-maxima wind structure during the 2008-2009 winter manifests as the growth of an unstable PW1.

761 The background flow evolution leading to SSW onset fostered wave geometry suitable
762 for wave over-reflection (c.f., Figure 1). With the formation of a double-maxima wind structure,
763 the polar jet core strengthened and migrated poleward as the wave evanescent layer around 0.01
764 hPa (seen in Figure 11) became thinner. The stronger polar jet guided the upward-propagating
765 PWs (see Figures 10 and 11) more vertically toward the thin evanescent region, increasing the
766 likelihood of over-reflection, particularly for EPWs. Notably, this polar wind evolution may also
767 provide the background wave geometry to favor SSW onset through resonance (e.g., Albers &
768 Birner, 2014).

769 The composite evolution of EPW1 and EPW2 revealed their growth in parallel with the
770 double-maxima wind configuration (see Figure 12). Local eastward accelerations due to flux
771 divergence near their wave sources generally occurred above the polar jet. Accompanied by
772 westward acceleration, the damping of EPW1 appeared on the equatorward and poleward side of
773 the polar jet core. In contrast, EPW2 damping led to westward acceleration on the poleward
774 flank of the subtropical jet.

775 EPWs appear to be mesospheric instability waves with overlapping characteristics of
776 over-reflection of upward-propagating PWs. While suitable wave geometry for over-reflection
777 exists throughout the winter, a double-maxima wind configuration increases the likelihood of
778 over-reflection. In reducing the preexisting wind shear and, thereby, stabilizing the polar jet,
779 EPWs can significantly impact the jet structure and may play a key role in the nature and timing
780 of SSW events.

781 **Acknowledgments**

782 CR is supported by funding from the National Science Foundation (NSF) awards (RUI
783 1642232; REU 1560210). VL is supported by NSF Intergovernmental Panel Agreement. YO is
784 supported in part by the Research Council of Norway/CoE under contract 223252/F50. The
785 authors acknowledge the computing and technical support from the NCAR Computation
786 Information Systems Laboratory as well as the Coastal Carolina University cyberinfrastructure
787 (CCU CI) project, funded in part by NSF award MRI 1624068. The relevant daily model output
788 can be accessed through the CCU CI at https://mirror.coastal.edu/sce. The MLS temperature and
789 geopotential height data can be retrieved from https://doi.org/10.5067/Aura/MLS/DATA2520
790 and https://doi.org/10.5067/Aura/MLS/DATA2507, respectively.

791 **References**

792 Albers, J. R., & Birner, T. (2014), Vortex Preconditioning due to Planetary and Gravity Waves
793 prior to Sudden Stratospheric Warmings. *Journal of the Atmospheric Sciences*, *71*, 4028–
794 4054. https://doi.org/10.1175/JAS-D-14-0026.1

795 Andrews, D. G., Holton, J. R., & Leovy, C. B. (1987), *Middle Atmosphere Dynamics*. San
796 Diego, California: Academic Press.

797 Baldwin, M. P., & Dunkerton, T. J. (2001), Stratospheric harbingers of anomalous weather
798 regimes. *Science*, *294*, 581–584. https://doi.org/10.1126/science.1063315

799 Butler, A. H., Seidel, D. J., Hardiman, S. C., Butchart, N., Birner, T., & Match, A. (2015),
800 Defining sudden stratospheric warmings. *Bulletin of the American Meteorological Society*,
801 (November), 1913–1928. https://doi.org/10.1175/BAMS-D-13-00173.1

Chandran, A., Garcia, R. R., Collins, R. L., & Chang, L. C. (2013), Secondary planetary waves in the middle and upper atmosphere following the stratospheric sudden warming event of January 2012. *Geophysical Research Letters*, *40*, 1861–1867. https://doi.org/10.1002/grl.50373

Charlton, A. J., & Polvani, L. M. (2007), A New Look at Stratospheric Sudden Warmings. Part I: Climatology and Modeling Benchmarks. *J. Climate*, *20*, 470–488. https://doi.org/10.1175/JCLI3994.1

Charney, J. G., & Eliassen, A. (1949), A Numerical Method for Predicting the Perturbations of the Middle Latitude Westerlies. *Tellus*, *1*, 38–54. https://doi.org/10.3402/tellusa.v1i2.8500

Coy, L., Eckermann, S. D., Hoppel, K. W., & Sassi, F. (2011), Mesospheric Precursors to the Major Stratospheric Sudden Warming of 2009: Validation and Dynamical Attribution Using a Ground-to-Edge-of-Space Data Assimilation System. *Journal of Advances in Modeling Earth Systems*, *3*, 1–7. https://doi.org/10.1029/2011MS000067

Coy, Lawrence, & Pawson, S. (2015), The major stratospheric sudden warming of January 2013: Analyses and forecasts in the GEOS-5 data assimilation system. *Monthly Weather Review*, *143*, 491–510. https://doi.org/10.1175/MWR-D-14-00023.1

Dickinson, R. E. (1973), Baroclinic Instability of an Unbounded Zonal Shear Flow in a Compressible Atmosphere. *J. Atmos. Sci.*, *30*, 1520–1527.

Duck, T. J., Whiteway, J. A., & Carswell, A. I. (2001), The Gravity Wave–Arctic Stratospheric Vortex Interaction. *Journal of the Atmospheric Sciences*, *58*(23), 3581–3596. https://doi.org/10.1175/1520-0469(2001)058<3581:TGWASV>2.0.CO;2

Ern, M., Preusse, P., Alexander, M. J., & Warner, C. D. (2004), Absolute values of gravity wave momentum flux derived from satellite data. *Journal of Geophysical Research D: Atmospheres*, *109*(20), 1–17. https://doi.org/10.1029/2004JD004752

Fetzer, E. J., & Gille, J. C. (1994), Gravity Wave Variance in LIMS Temperatures. Part I: Variability and Comparison with Background Winds. *Journal of the Atmospheric Sciences*. https://doi.org/10.1175/1520-0469(1994)051<2461:gwvilt>2.0.co;2

Gelaro, R., McCarty, W., Suárez, M. J., Todling, R., Molod, A., Takacs, L., et al. (2017), The modern-era retrospective analysis for research and applications, version 2 (MERRA-2). *Journal of Climate*, *30*, 5419–5454. https://doi.org/10.1175/JCLI-D-16-0758.1

Goncharenko, L. P., Chau, J. L., Liu, H. L., & Coster, A. J. (2010), Unexpected connections between the stratosphere and ionosphere. *Geophysical Research Letters*, *37*(L10101). https://doi.org/10.1029/2010GL043125

Harada, Y., Goto, A., Hasegawa, H., Fujikawa, N., Naoe, H., & Hirooka, T. (2010), A major stratospheric sudden warming event in January 2009. *Journal of the Atmospheric Sciences*, *67*, 2052–2069. https://doi.org/10.1175/2009JAS3320.1

Harnik, N., & Heifetz, E. (2007), Relating overreflection and wave geometry to the counterpropagating Rossby wave perspective: Toward a deeper mechanistic understanding of shear instability. *Journal of the Atmospheric Sciences*, *64*, 2238–2261. https://doi.org/10.1175/JAS3944.1

Hartmann, D. L. (1983), Barotropic Instability of the Polar Night Jet Stream. *J. Atmos. Sci.*

https://doi.org/10.1175/1520-0469(1983)040%3C0817:BIOTPN%3E2.0.CO;2

Iida, C., Hirooka, T., & Eguchi, N. (2014), Circulation changes in the stratosphere and mesosphere during the stratospheric sudden warming event in January 2009. *Journal of Geophysical Research*, *119*, 7104–7115. https://doi.org/10.1002/2013JD021252

Kuttippurath, J., & Nikulin, G. (2012), A comparative study of the major sudden stratospheric warmings in the Arctic winters 2003/2004-2009/2010. *Atmospheric Chemistry and Physics*, *12*, 8115–8129. https://doi.org/10.5194/acp-12-8115-2012

Leovy, C. (1964), Simple models of thermally driven mesospheric circulation. *Journal of Atmospheric Sciences*, *21*(4), 327–341.

Leovy, C. B., & Webster, P. J. (1976), Stratospheric long waves - Comparison of thermal structure in the Northern and Southern Hemispheres. *Journal of Atmospheric Sciences*, *33*, 1624–1638. https://doi.org/doi:10.1175/1520-0469(1976)033<1624:SLWCOT>2.0.CO;2

Limpasuvan, V., Richter, J. H., Orsolini, Y. J., Stordal, F., & Kvissel, O. K. (2012), The roles of planetary and gravity waves during a major stratospheric sudden warming as characterized in WACCM. *Journal of Atmospheric and Solar-Terrestrial Physics*, *78–79*, 84–98. https://doi.org/10.1016/j.jastp.2011.03.004

Limpasuvan, V., Orsolini, Y. J., Chandran, A., Garcia, R. R., & Smith, A. K. (2016), On the composite response of the MLT to major sudden stratospheric warming events with elevated stratopause. *Journal of Geophysical Research*, *121*, 4518–4537. https://doi.org/10.1002/2015JD024401

Lindzen, R. S., Farrell, B., & Tung, K. K. (1980), The concept of wave overreflection and its application to baroclinic instability. *Journal of the Atmospheric Sciences*, *37*, 44–63. https://doi.org/10.1175/1520-0469(1980)037<0044:TCOWOA>2.0.CO;2

Lindzen, Richard S. (1988), Instability of Plane Parallel Shear Flow. *Pageoph*, *126*(1), 103–121.

Livesey, N. J., Read, W. G., Wagner, L. F., Lambert, A., Manney, G. L., Valle, L. F. M., et al. (2017), *Earth Observing System (EOS) Microwave Limb Sounder (MLS) Verson 4.2x Level 2 data quality and description document. JPL D-33509 Rev. D*. Pasadena, California: Jet Propulsion Laboratory, California Institute of Technology.

Manney, G. L., Krüger, K., Pawson, S., Minschwaner, K., Schwartz, M. J., Daffer, W. H., et al. (2008), The evolution of the stratopause during the 2006 major warming: Satellite data and assimilated meteorological analyses. *Journal of Geophysical Research*, *113*(D11115), 1–16. https://doi.org/10.1029/2007jd009097

Manney, G. L., Schwartz, M. J., Krüger, K., Santee, M. L., Pawson, S., Lee, J. N., et al. (2009), Aura Microwave Limb Sounder observations of dynamics and transport during the record-breaking 2009 Arctic stratospheric major warming. *Geophysical Research Letters*, *36*(12), 1–5. https://doi.org/10.1029/2009GL038586

Manny, G. L., Nathan, T. R., & Stanford, J. L. (1988), Barotropic stability of realistic stratospheric jets. *Journal of Atmospheric Sciences*, *45*(18), 2545–2555.

Marsh, D. R., Mills, M. J., Kinnison, D. E., Lamarque, J. F., Calvo, N., & Polvani, L. M. (2013), Climate change from 1850 to 2005 simulated in CESM1(WACCM). *Journal of Climate*, *26*, 7372–7391. https://doi.org/10.1175/JCLI-D-12-00558.1

Matsuno, T. (1971), A dynamical model of stratospheric sudden warming. , 1479–1494. Retrieved from http://journals.ametsoc.org/doi/pdf/10.1175/1520-0469%281971%29028%3C1479%3AADMOTS%3E2.0.CO%3B2

Matthias, V., & Ern, M. (2018), On the origin of the mesospheric quasi-stationary planetary waves in the unusual Arctic winter 2015/2016. *Atmospheric Chemistry and Physics*, *18*(7), 4803–4815. https://doi.org/10.5194/acp-18-4803-2018

O'Neill, A., & Youngblut, C. E. (1982), Stratospheric Warmings Diagnosed Using the Transformed Eulerian-Mean Equations and the Effect of the Mean State on Wave Propagation. *Journal of the Atmospheric Sciences*, *39*, 1370–1386. https://doi.org/10.1175/1520-0469(1982)039<1370:swdutt>2.0.co;2

Orsolini, Y., & Simon, P. (1995), Idealized life cycles of planetary-scale barotropic waves in the middle atmosphere. *Journal of the Atmospheric Sciences*, *52*(22), 3817–3835.

Pedatella, N. M., Oberheide, J., Sutton, E. K., Liu, H., Anderson, J. L., & Raeder, K. (2016), Journal of Geophysical Research : Space Physics Short-term nonmigrating tide variability in the mesosphere , thermosphere , and ionosphere. *Journal of Geophysical Research: Space Physics*, *121*, 3621–3633. https://doi.org/10.1002/2016JA022528.Received

Pedlosky, J. (1987), *Geophysical Fluid Dynamics*. (2nd ed.). New York: Springer.

Richter, J. H., Sassi, F., & Garcia, R. R. (2010), Toward a Physically Based Gravity Wave Source Parameterization in a General Circulation Model. *Journal of the Atmospheric Sciences*, *67*, 136–156. https://doi.org/10.1175/2009JAS3112.1

Rüfenacht, R., Baumgarten, G., Hildebrand, J., Schranz, F., Matthias, V., Stober, G., et al. (2018), Intercomparison of middle-atmospheric wind in observations and models. *Atmospheric Measurement Techniques*, *11*, 1971–1987. https://doi.org/10.5194/amt-11-1971-2018

Salby, M. L. (1996), *Fundamentals of Atmospheric Physics*. . San Diego, California: Academic Press.

Sassi, F., Liu, H. L., & Emmert, J. T. (2016), Traveling planetary-scale waves in the lower thermosphere: Effects on neutral density and composition during solar minimum conditions. *Journal of Geophysical Research A: Space Physics*, *121*, 1780–1801. https://doi.org/10.1002/2015JA022082

Scherhag, R. (1952), Die explosionsartigen Stratosphärenerwärmungen des Spätwinter 1951/1952 (The explosive warmings in the stratosphere of the late winter 1951/1952). *Ber. Dtsch. Wetterdienstes U.S. Zone*, *38*, 51–63.

Smagorinsky, J. (1953), The dynamical influence of large-scale heat sources and sinks on the quasi-stationary mean motions of the atmosphere. *Quarterly Journal of the Royal Meteorological Society*, *79*, 342–366.

Solomon, S., Garcia, R. R., Olivero, J. J., Bevilacqua, R. M., Schwartz, P. R., Clancy, R. T., & Muhleman, D. O. (1985), Photochemistry and Transport of Carbon Monoxide in the Middle Atmosphere. *Journal of Atmospheric Sciences*, *42*(10), 1072–1083.

De Wit, R. J., Hibbins, R. E., Espy, P. J., Orsolini, Y. J., Limpasuvan, V., & Kinnison, D. E. (2014), Observations of gravity wave forcing of the mesopause region during the January

2013 major Sudden Stratospheric Warming. *Geophysical Research Letters*, *41*, 4745–4752. https://doi.org/10.1002/2014GL060501